Article

Neuron

Feedback-Driven Mechanisms between Microtubules and the Endoplasmic Reticulum Instruct Neuronal Polarity

Highlights

- ER tubules localize to the axon, and ER cisternae are retained in the soma
- Localization of axonal ER depends on ER-shaping proteins and the MT cytoskeleton
- ER-MT crosstalk stabilizes both ER tubules and MTs in the axon
- ER-MT crosstalk is critical for neuronal polarity

Authors

Ginny G. Farías, Amélie Fréal, Elena Tortosa, ..., Lena Will, Maarten Altelaar, Casper C. Hoogenraad

Correspondence

g.c.fariasgaldames@uu.nl (G.G.F.), c.hoogenraad@uu.nl (C.C.H.)

In Brief

Farías et al. report that the localization of the endoplasmic reticulum (ER) in the axon is controlled by the interaction between ER-shaping proteins and the microtubule cytoskeleton. Local ER and microtubule crosstalk promotes ER tubule-microtubule stabilization and drives neuronal polarity.

Farías et al., 2019, Neuron *102*, 184–201
April 3, 2019
https://doi.org/10.1016/j.neuron.2019.01.030

CellPress

CellPress

Neuron
Article

Feedback-Driven Mechanisms between Microtubules and the Endoplasmic Reticulum Instruct Neuronal Polarity

Ginny G. Farías,[1,*] Amélie Fréal,[1] Elena Tortosa,[1] Riccardo Stucchi,[1,2] Xingxiu Pan,[1] Sybren Portegies,[1] Lena Will,[1] Maarten Altelaar,[2] and Casper C. Hoogenraad[1,3,*]

[1]Cell Biology, Department of Biology, Faculty of Science, Utrecht University, Utrecht 3584 CH, the Netherlands

[2]Biomolecular Mass Spectrometry and Proteomics, Bijvoet Center for Biomolecular Research and Utrecht Institute for Pharmaceutical Sciences, Utrecht University, 3584 CH Utrecht, the Netherlands

[3]Lead Contact

*Correspondence: g.c.fariasgaldames@uu.nl (G.G.F.), c.hoogenraad@uu.nl (C.C.H.)

https://doi.org/10.1016/j.neuron.2019.01.030

SUMMARY

Establishment of neuronal polarity depends on local microtubule (MT) reorganization. The endoplasmic reticulum (ER) consists of cisternae and tubules and, like MTs, forms an extensive network throughout the entire cell. How the two networks interact and control neuronal development is an outstanding question. Here we show that the interplay between MTs and the ER is essential for neuronal polarity. ER tubules localize within the axon, whereas ER cisternae are retained in the somatodendritic domain. MTs are essential for axonal ER tubule stabilization, and, reciprocally, the ER is required for stabilizing and organizing axonal MTs. Recruitment of ER tubules into one minor neurite initiates axon formation, whereas ER retention in the perinuclear area or disruption of ER tubules prevent neuronal polarization. The ER-shaping protein P180, present in axonal ER tubules, controls axon specification by regulating local MT remodeling. We propose a model in which feedback-driven regulation between the ER and MTs instructs neuronal polarity.

INTRODUCTION

Neuronal function relies on the proper formation and maintenance of two highly asymmetric structures, the somatodendritic and axonal domains, which contain different compositions of proteins and organelles. During neuronal development, axon formation is the initial step in establishing neuronal polarity, followed by the development of dendrites and polarized cargo sorting into neuronal components. Local rearrangement of the cytoskeleton is the major determinant in breaking symmetry, in which reorganization of a stable and uniform pool of parallel microtubule (MT) bundles is required for axon formation and maintenance of neuronal polarity (Kapitein and Hoogenraad, 2015). Microtubule-associated proteins (MAPs) have been proposed to be major players in regulating MT remodeling in the axon (Conde and Cáceres, 2009). Cumulating evidence indicates that specific membrane proteins, resident in the endoplasmic reticulum (ER), have the ability to directly bind MTs and regulate their organization and stability (Gurel et al., 2014). In addition, several mutations in ER-resident proteins have been reported to cause the neurological disorder spastic paraplegia, characterized by MT disorganization and severe axonal degeneration (Blackstone, 2012; Goyal and Blackstone, 2013), highlighting the relevance of axonal ER organization in neuronal function. However, little is known about the interplay between MTs and the ER in neurons.

The ER is one of the largest organelles in mammalian cells and, like the MT cytoskeleton, forms an extensive network filling the entire cell. The ER is organized into two distinct structural and functional interconnected domains determined by the shape of their membranes: ER cisternae and ER tubules. In unpolarized cells, the ER distributes as perinuclear ER cisternae and peripheral ER tubules that interact with each other, forming tubular junctions or more complex dense ER tubular matrices (Shibata et al., 2006; Nixon-Abell et al., 2016). In mature neurons, the ER distributes along the entire axon as mainly a tubular organization (Wu et al., 2017). Specific ER-resident transmembrane proteins control the shape of the ER. For instance, ER-shaping proteins such as CLIMP63, P180 (also known as ribosome binding protein 1 homolog 180-kDa [RRBP1]), and kinectin (KTN1) induce a flattened structure organization of ER cisternae (Shibata et al., 2010), whereas proteins such as reticulons (RTNs) and DP1 (also known as REEP5) promote high curvature of ER membranes to form ER tubules (Voeltz et al., 2006).

Although ER membranes *in vitro* can form a reticular network without MTs (Dreier and Rapoport, 2000), it is generally believed that the interaction between the ER and MTs regulates the shape of the ER. For instance, nocodazole-induced MT depolymerization leads to the retraction of peripheral ER tubules and their interconversion to perinuclear ER cisternae (Terasaki et al., 1986). The MT plus-end motor KIF5 as well as the MT end-binding protein 1 (EB1) regulate ER tubule localization at the cell periphery, whereas the MT minus-end motor dynein transports ER tubules backward to the perinuclear area (Waterman-Storer and Salmon, 1998; Grigoriev et al., 2008; Woźniak et al., 2009). Several ER transmembrane proteins, such as CLIMP63, P180, REEP1, and Sec61β, have been shown to directly interact

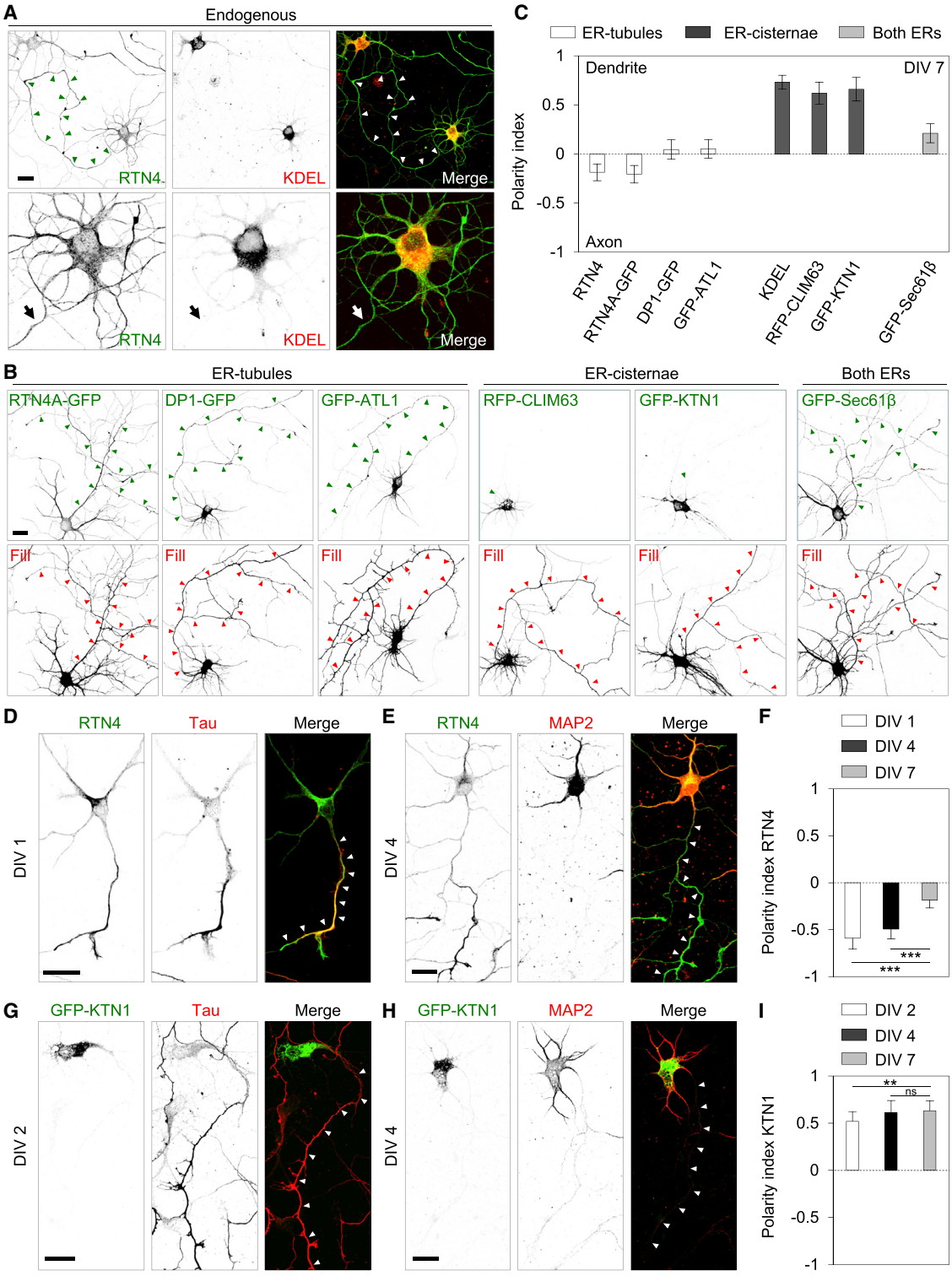

Figure 1. ER Tubules Preferentially Target the Axon, whereas ER Cisternae Are Restricted to the Somatodendritic Domain

(A) Representative images of DIV7 hippocampal neurons stained with antibodies against endogenous RTN4 protein (green) and the KDEL signal peptide (red). Bottom: higher magnifications.

(B) Representative images of DIV7 neurons transfected on DIV5 with different ER tubule and ER cisterna markers tagged with GFP or RFP (green) plus fill (fluorescently tagged empty vector, red).

(legend continued on next page)

with MTs (Klopfenstein et al., 1998; Ogawa-Goto et al., 2007; Park et al., 2010; Zhu et al., 2018). Although the functional relevance of this interactions is not fully understood, MTs may play a role in locally immobilizing the ER to drive efficient protein synthesis (Nikonov et al., 2007; Ogawa-Goto et al., 2007; Zhu et al., 2018). In addition, some of these factors (e.g., P180, Sec61β, and REEP1) have also been shown to control MT organization (Ogawa-Goto et al., 2007; Park et al., 2010; Zhu et al., 2018). However, the role of MT-ER interactions in developing neurons is an outstanding question.

Here we found that ER tubules localize to the axon at very early stages of neuronal development. The localization of the axonal ER depends on the MT plus-end motor KIF5 and ER tubule-shaping proteins. We also show that the crosstalk between the ER and axonal MTs is decisive for neuronal polarity. Disrupting the MT cytoskeleton alters ER tubule organization, and alterations in the ER disrupt proper MT organization and axon initiation. In unpolarized neurons, recruitment of ER tubules into one neurite initiates axon formation, whereas ER retention in the perinuclear area or disruption of ER tubules prevents neuronal polarization. Finally, we demonstrated that ER tubules containing the ER-shaping protein P180 control axon formation by inducing MT stabilization. Our data indicate that the interplay between the ER and MTs is critical for axonal specification and neuronal polarity.

RESULTS

ER Tubules and ER Cisternae Have a Distinct Distribution in Developing Neurons

To determine how the ER is organized in neurons, we first analyzed the distribution of various endogenous and overexpressed ER-resident proteins in primary cultures of rat hippocampal neurons at day *in vitro* 7 (DIV7). Immunofluorescent staining for endogenous RTN4 (a protein enriched in ER tubules) localized to the somatodendritic and axonal domains but was slightly more abundant in the distal region of the axon (Figure 1A). In contrast, staining for endogenous KDEL (a sequence abundant in some ER cisterna-resident proteins) was most concentrated in the soma, present in dendrites, but excluded from the axon (Figure 1A).

Next, we analyzed the distribution of low expression levels of several fluorescently tagged ER-resident proteins, which are more abundant in ER tubules (RTN4A, DP1, and ATL1) and ER cisternae (CLIMP63 and KTN1) or present in both ER compartments (Sec61β) in polarized neurons. Sec61β, RTN4A, DP1, and ATL1 were all distributed in dendrites and the axon (Figure 1B). However, CLIMP63 and KTN1 were excluded from the axon (Figure 1B). Quantification of the polarity index (PI; [intensity dendrite − intensity axon] / [intensity dendrite + intensity axon]) of these endogenous and overexpressed ER proteins confirmed the unpolarized distribution of ER tubule proteins (PI, −0.2 to 0) and the somatodendritic distribution of ER cisterna proteins (PI, 0.6 to 0.7) in fully polarized neurons at DIV7 (Figure 1C). The slightly more abundant Sec61β in dendrites (PI, ∼0.2) was consistent with the presence of both ER tubules and ER cisternae in dendrites (Figures 1B and 1C).

To determine whether ER tubules require complete neuronal polarization to access the axon, we studied the distribution of endogenous RTN4 in neurons in early stages of development. DIV1 and DIV4 hippocampal neurons showed axonal distribution of RTN4, as evidenced by its co-distribution with the axonal marker Tau at DIV1 (Figure 1D) and by its presence in axons negative for the somatodendritic marker MAP2 at DIV4 (Figure 1E). Interestingly, quantification of the polarity index for endogenous RTN4 revealed that ER tubules were preferentially targeted to the axon before neurons reached a fully polarized organization (PI: ∼-0.6 on DIV1, ∼-0.5 on DIV4, and ∼-0.2 on DIV7; Figure 1F). In contrast, ER cisternae containing GFP-KTN1 were excluded from the axon in all of these stages (Figures 1G–1I). Together, these results show that the different domains of the ER, tubules and cisternae, have a distinct distribution in developing neurons.

MT-Based Transport and ER-Shaping Proteins Control Axonal ER Distribution

The MT-driven motor KIF5 and dynein as well as the MT end-binding protein 1 (EB1) have been shown to transport ER tubules between the perinuclear area and the cell periphery in non-neuronal cells (Waterman-Storer and Salmon; 1998; Grigoriev et al., 2008; Woźniak et al., 2009). Here we examined whether these mechanisms also contribute to the axonal distribution of the ER. To address this question, we transfected neurons with plasmids containing short hairpin RNA (shRNA) sequences targeting KIF5 (isoforms A, B, and C), the subunit P150 of the dynein complex, and EB (isoforms 1 and 3) proteins and analyzed the distribution of RTN4A-GFP in DIV7 neurons. Knockdown of KIF5 showed reduced axonal distribution of ER tubules and more abundance of them in the somatodendritic domain (PI, ∼0.7; Figures 2A and 2B). In contrast, knockdown of P150 caused accumulation of ER tubules in the distal axon (PI, ∼−0.5; Figures 2A and 2B), whereas shRNAs targeting EBs reduced only dendritic ER tubule distribution (Figures 2A and 2B). shRNA directed to KIF1A, another MT plus-end-directed motor, did not affect ER tubule distribution (Figure 2B). These results indicate that KIF5 and dynein are the main MT-driven proteins responsible for the antero- and retrograde transport of ER tubules in the axon, respectively. To determine whether ER cisternae are removed by the axon by active dynein-mediated transport, we knocked down P150 and

(C) Polarity indexes of the different ER-resident proteins in (A) and (B) at DIV7; n = 15–20 neurons per condition.
(D–F) Representative images of neurons co-stained for endogenous RTN4 (green) together with Tau (red) at DIV1 (D) or MAP2 (red) at DIV4 (E) and polarity indexes for endogenous RTN4 at DIV1, DIV4, and DIV7 (F); n = 30 neurons per condition.
(G–I) Representatives images of neurons transfected with GFP-KTN1 on DIV1, stained as in (D) and (E) at DIV2 (G) and DIV4 (H), and polarity indexes for GFP-KTN1 at DIV2, DIV4, and DIV7 (I); n = 20 neurons per condition.
Red and white arrowheads point to the axon, green arrowheads point to the axonal ER, and arrows point to the proximal axon. Scale bars represent 20 μm in all images. In all graphs, values correspond to the mean ± SD. ns, not significant; ***$p < 0.001$ and **$p < 0.01$ comparing conditions in DIV1 and DIV2 and DIV4 to DIV7 in (F) and (I) (Kruskal-Wallis test followed by a Dunn's multiple comparisons test).

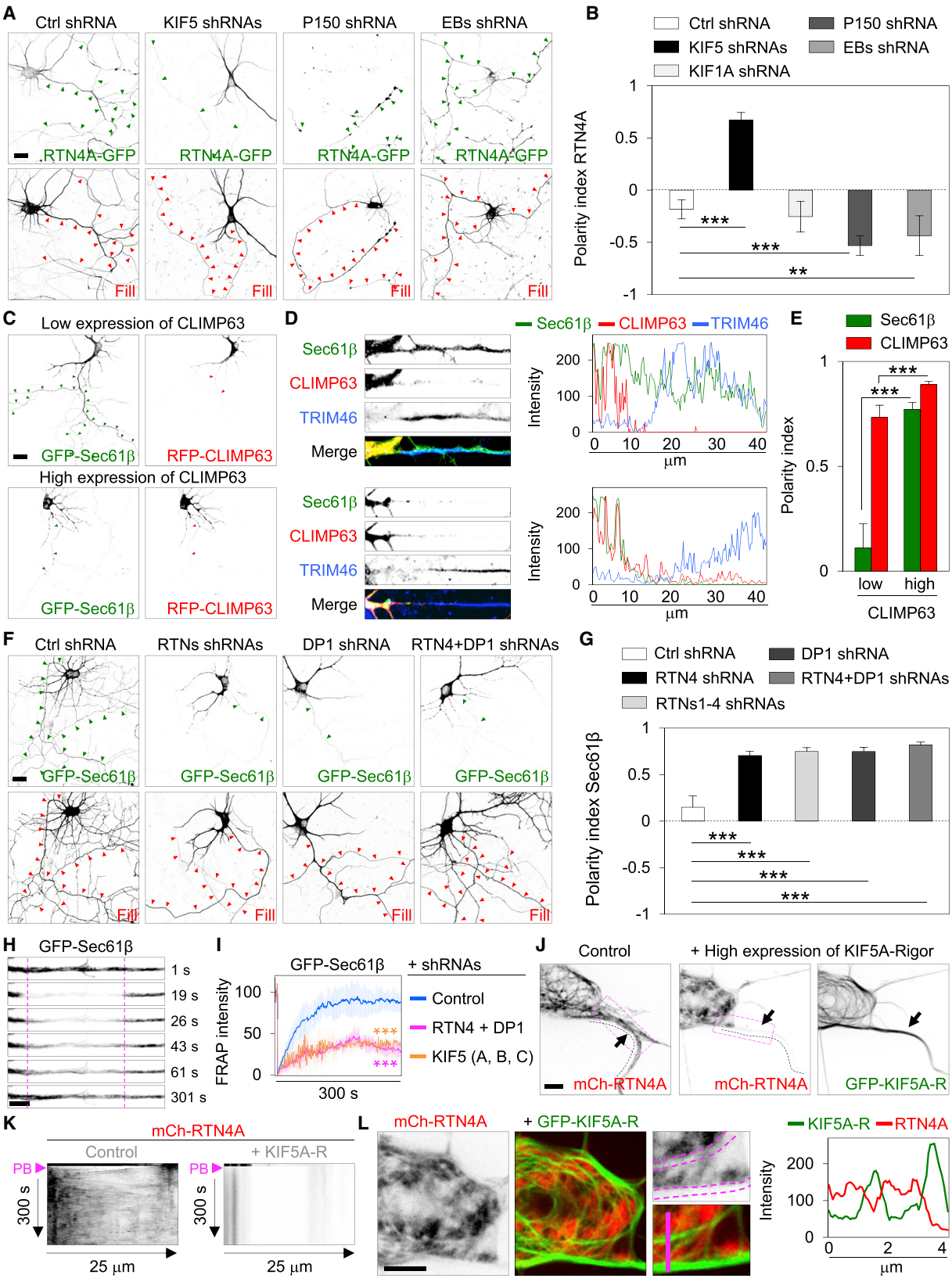

(legend on next page)

compared the accumulation of ER tubule, ER cisterna, and general ER markers in the axon tips respective to their controls. RTN4 and Sec61β showed an ~6- and ~3.5-fold increase, respectively, whereas CLIMP63 was not detected in axon tips (Figure S1A). This result indicates that only ER tubules can access the axon and that ER cisternae are excluded from the axon more than actively retrograde-transported back to the soma.

Next, we investigated whether the balance between ER tubules and ER cisternae could also contribute to the abundance of ERs in the axon. We first analyzed the distribution of the general ER-resident marker GFP-Sec61β in neurons expressing low and high levels of the ER cisterna-shaping protein CLIMP63. RFP-CLIMP63 was mainly distributed in the somatodendritic domain and excluded from the axon in both low- and high-expressing neurons (PI, ~0.7 and ~0.9, respectively; Figures 2C–2E). However, the axonal distribution of GFP-Sec61β was disrupted in neurons expressing high levels of CLIMP63, as evidenced by its dramatic shift to a restrictive somatodendritic distribution (PI, ~0.2 to ~0.8), which can be explained by a reduction of axonal ER tubules and an expansion of ER cisternae along the dendrites but not the axon (Figures 2C–2E).

To study whether ER tubule-shaping proteins also affect the abundance of ERs in the axon, we first designed and confirmed the efficiency of shRNAs targeting RTNs 1–4 and DP1 in neurons nucleofected on DIV0 and analyzed on DIV4 by mass spectrometry (Figure S3). Then we transfected different combinations of shRNAs for RTNs and DP1 and analyzed the distribution of GFP-Sec61β in DIV7 neurons. Knocking down all four RTN isoforms as well as only RTN4 (the most abundant RTN isoform in neurons; Figure S3C) caused a shift in Sec61β from almost unpolarized to a mainly somatodendritic distribution (PI, ~0.2 control to ~0.7 shRNAs; Figures 2F and 2G). Similar results were obtained for DP1 knockdown (PI, ~0.7), and a more dramatic shift in Sec61β distribution was observed in neurons knocked down for both RTN4 and DP1 (PI, ~0.8; Figures 2F and 2G). In contrast, knockdown of the ER cisterna-shaping protein CLIMP63 or CLIMP63 plus KTN1 increased the abundance of Sec61β in the axon (PI, ~−0.4 and ~−0.5, respectively) (Figure S1B).

To further analyze the dynamics of the axonal ER, we performed-live cell imaging and fluorescence recovery after photobleaching (FRAP) of GFP-Sec61β in the axons of DIV7 neurons. Anterograde and retrograde movement of ER tubules was observed after photobleaching in control neurons, with ~85% recovery of the mean fluorescence intensity within 5 min (Figures 2H and 2I; Video S1). However, axons from neurons knocked down for KIF5 as well as for RTN4 plus DP1 showed reduced Sec61β mean intensity recovery compared with control neurons (Figure 2I). Similar ER movement in control neurons stained with the ER-BODIPY-red tracker was observed (Figure S2C). By using the classical ER membrane marker DiOC6, we also confirmed that the reduction of Sec61β in axons from neurons knocked down for KIF5 or RTN4 plus DP1 or high expression of CLIMP63 is due to a reduction of the ER tubule membrane itself (Figures S2A and S2B).

In addition, we evaluated ER distribution in the presence of a KIF5A-rigor mutant that can bind MTs but not walk or dissociate from them (Farías et al., 2015). High expression of the GFP-KIF5A-rigor mutant prevented access of mCh-RTN4A to the axon compared with control neurons in which ER tubules entering the axon were clearly observed after photobleaching (Figures 2J and 2K; Video S2). Similarly, KIF5A-rigor also prevented entrance of the ER-BODIPY-red tracker and mCh-Sec61β to the axon (Figure S2D). Together, these results indicate that MT-based transport and the shape of the ER control the distribution of the ER in the axon.

MT-ER Interaction Regulates ER Organization and Distribution in Neurons

We found that KIF5A-rigor was not only altering the KIF5-based transport of ER tubules to the axon but also blocking the ER-MT interaction and affecting ER shape. KIF5A-rigor caused interconversion of ER tubules to ER cisternae, which were clearly excluded from MT bundles occupied by KIF5A-rigor (Figure 2L; Figure S2E; Video S2). Because KIF5A-rigor binds preferentially

Figure 2. MT-Based Transport and ER-Shaping Proteins Control Axonal Distribution of the ER

(A) Representative images of DIV7 neurons co-transfected on DIV4 with RTN4A-GFP (top) plus fill (bottom) and the pSuper empty plasmid (control) or the same plasmid containing shRNA sequences targeting KIF5 (isoforms A, B, and C), P150, or EBs (isoforms 1 and 3).

(B) Polarity indexes of RTN4A-GFP in the presence of KIF5, KIF1A, P150, or EB shRNAs; n = 20 neurons.

(C–E) Representative images of neurons expressing GFP-Sec61β in the presence of low (top) or high (bottom) expression levels of RFP-CLIMP63 (C). Also shown are straightened regions from their proximal axon (left) with their respective diagrams of the average fluorescence intensity profiles for GFP-Sec61β (green), RFP-CLIMP63 (red), and the proximal axonal marker TRIM46 (blue) (D, right) and polarity indexes of Sec61β and CLIMP63 (E). n = 15 neurons per condition.

(F and G) Representative images of DIV7 neurons co-transfected on DIV4 with GFP-Sec61β (top) plus fill (bottom) together with a control plasmid or shRNAs directed to RTN1–RTN4, DP1, and RTN4 plus DP1 (F). Also shown are polarity indexes of GFP-Sec61β in neurons expressing shRNAs for RTN4, RTN1–RTN4, DP1, or RTN4 plus DP1 (G). n = 20 neurons per condition.

(H) Representative still images of a straightened proximal axon region from a live neuron expressing GFP-Sec61β photobleached in the indicated area and recorded for 300 s. See also Video S1.

(I) Average normalized intensity graph for FRAP of GFP-Sec61β performed as in (H) of neurons co-expressing shRNAs against RNT4 plus DP1, KIF5, or empty pSuper vector (control). n = 9, 8, and 11 neurons, respectively.

(J–L) Representative still images from live neurons expressing only mCh-RTN4A (control) or mCh-RTN4A plus GFP-KIF5A-rigor at time 0 s (J). Kymographs from straightened proximal axon regions from the dashed line in (J) are shown in (K). FRAP region and photobleaching (PB) time are indicated in magenta in (J) and (K), respectively. Also shown are higher magnifications and merged images of a neuron expressing mCh-RTN4A plus GFP-KIF5A-R and a diagram of the average fluorescence intensity profiles for mCh-RTN4A (red) and KIF5A-rigor (green) from the indicated solid magenta line in (L). See also Video S2.

Green and red arrowheads point to the axonal ER or to the axonal domain, respectively, in (A) and (F). Scale bars represent 20 μm in (A), (C), and (F) and 5 μm in (H), (J), and (L). In the graphs in (B), (E), and (G) mean ± SD is shown. ***p < 0.001 and **p < 0.01, comparing individual conditions with the control; Kruskal-Wallis test followed by a Dunn's multiple comparisons test in (B); one-way ANOVA followed by Dunnett's multiple comparisons test in (E) and (G). See also Figures S1–S3.

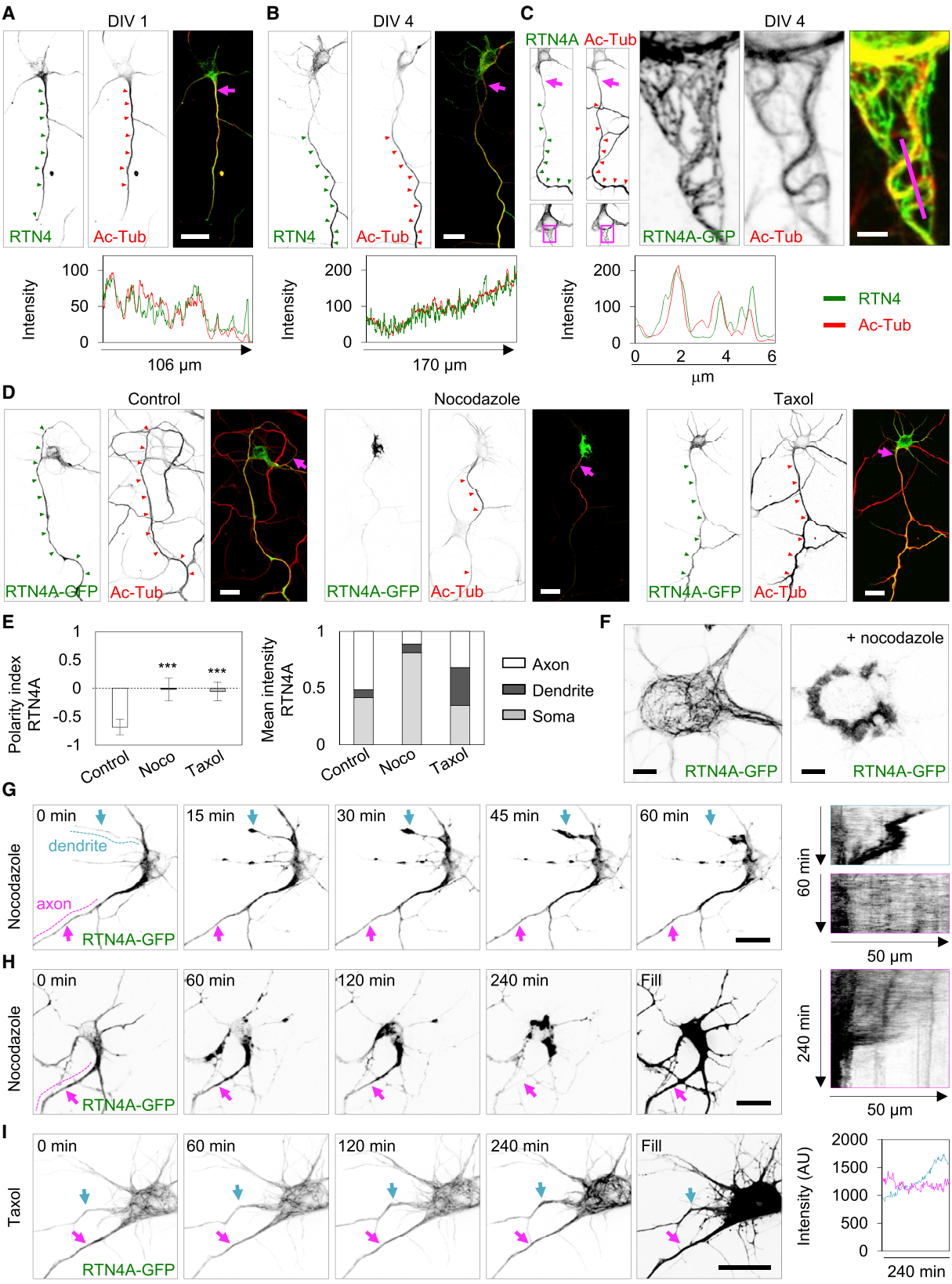

(legend on next page)

to stable acetylated MTs in neurons (Farías et al., 2015), we analyzed the co-distribution of the ER and acetylated MTs at different stages of development. A preferential co-distribution of endogenous RTN4 and acetylated α-tubulin along the axon was observed in DIV1 and DIV4 neurons (Figures 3A and 3B). In the soma of neurons expressing high levels of RTN4A-GFP, we also visualized individual ER tubules colocalizing with stable acetylated MT bundles (Figure 3C). By using the MT-destabilizing and -stabilizing drugs nocodazole and Taxol, respectively, we then studied how the stability of MTs contributes to ER distribution and organization. DIV4 neurons exposed to 10 μM nocodazole for 4 h caused a reduction in the density of acetylated MTs along the medium and distal axon together with a drastic reduction in RTN4A-GFP in the axon and its accumulation, mainly in the soma (Figures 3D and 3E). Conversely, 20 nM Taxol produced an increase in RTN4A-GFP along the dendrites after 4 h of treatment (Figures 3D and 3E). Interestingly, nocodazole also caused the interconversion of ER tubules to ER cisternae in the soma (Figure 3F). The reduction of axonal ER tubules by nocodazole was also observed with GFP-Sec61β and DiOC6 markers (Figure S4A).

Then we analyzed the dynamics of ER redistribution in the presence of nocodazole and Taxol. Nocodazole induces time-dependent depolymerization of MTs, affecting first-dynamics MTs and later stable MTs (Baas et al., 2016). Nocodazole induced rapid redistribution and accumulation of RTN4A-GFP to the dendritic tips after 5–15 min to then start moving back to the soma after 30–120 min (Figures 3G and 3H; Video S3). Axonal RTN4A-GFP as well as GFP-Sec61β were still present in the imaged proximal axon after 1–2 h of treatment but drastically redistributed to the soma after 2–4 h (Figure 3G; Figure S4B; Video S3). On the other hand, Taxol did not affect the distribution of ER tubules in the first 2 h but started to slightly increase the abundance of them in the soma and dendrites after 3–4 h (Figure 3I; Video S3). These results indicate that MT stability contributes to ER distribution and organization in neurons.

ER Tubules Regulate MT Organization in Neurons

Conversely, we wondered whether ER tubules could have a role in MT organization and dynamics. To study this, we developed two strategies to manipulate ER tubule positioning. We induced acute and controlled depletion of ER tubules in the axon and sustained retention of ER tubules in the somatodendritic domain by using the FKBP-FRB rapalog-induced system and the Streptavidin-SBP (Streptavidin binding protein) heterodimerization system, respectively (Kapitein et al., 2010; Farías et al., 2017). More specifically, we triggered binding of the dynein motor complex to ER tubules by fusing an FRB sequence to a hemagglutinin (HA)-tagged BicD2 (a dynein cargo adaptor) and an FKBP sequence to GFP- or mCh-tagged RTN4A (Figure 4A). Only the addition of rapalog to neurons transfected with the above constructs caused removal of most ER tubules containing RTN4A in the axon after 1 h of treatment compared with neurons treated with just vehicle (Figure 4A). Similarly, adding a Streptavidin sequence to KIFC1 (another minus end-driven motor) and an SBP to RTN4A caused sustained retention of ER tubules in the somatodendritic domain and removal from the axon for several hours (24–48 h; Figure 4B). Axonal depletion of membranes containing RTN4A corresponded to ER tubules, as shown by the removal of other ER markers such as DiOC6, Sec61β, DP1, and ATL1 and endogenous RTN4 from the axons of transfected neurons treated with rapalog for 1 h (Figure 4C; Figures S5A–S5D).

By using the FKBP-FRB rapalog-induced system, we first found that the MT-binding and bundle protein TRIM46 (enriched in the proximal axon) (van Beuningen et al., 2015) was shifted to the soma and decorated a track of MTs running from the perinuclear area (where ER tubules were mostly re-distributed) to the very proximal axon (Figure 4D). Similar results were obtained with the Streptavidin-SBP system (Figure 4D). In addition, live-cell imaging of RFP-TRIM46 in neurons expressing GFP-FKBP-RTN4A plus HA-BicD-FRB indicated that the shift of TRIM46 to the soma started a few minutes after rapalog incubation, whereas TRIM46 was still immobile in the proximal axon after 1 h of recording in untreated neurons (Figure 4E; Video S4A). Then we analyzed the distribution of endogenous EB1 and dynamics of GFP-MT+TIP, both markers for dynamic MTs, in neurons expressing the rapalog system. Retraction of ER tubules to the perinuclear area caused a drastic increase in the number of the characteristic comets marking MT plus-end tips in regions of the soma that were lacking ER tubules, indicating an increase in MT instability (Figures 4F and 4G; Figure S5E; Video S5A). We also studied the distribution of CAMPSAP2, a non-centrosomal MT minus end-stabilizing protein that

Figure 3. MT Stability Regulates ER Distribution and Organization

(A and B) Representative images of neurons stained for RTN4 (green) and acetylated α-tubulin (Ac-Tub, red) at DIV1 (A) and DIV4 (B) and respective diagrams corresponding to the average fluorescence intensity profiles for their straightened axons (bottom).

(C) Representative image of a DIV4 neuron expressing RTNA-GFP (green) stained for Ac-Tub (red). An image of the soma from the same neuron indicates the enlarged region shown on the right. The diagram at the bottom corresponds to the average fluorescence intensity profiles in the traced magenta line.

(D) Representatives images of DIV4 neurons expressing RTN4-GFP, stained for Ac-Tub, and treated with 10 μM nocodazole, 20 nM Taxol, or vehicle (0.1% DMSO) for 4 h.

(E) Polarity indexes of RTN4A (left) and mean intensity for RTN4A in axons, dendrites, and soma with respect to total mean intensity (value 1) (right). n = 25 neurons per condition; the graph (left) shows mean ± SD. ***$p < 0.001$, comparing individual conditions with the control (Kruskal-Wallis test followed by Dunn's multiple comparisons test) (E).

(F) Representative images of the soma of DIV4 neurons expressing RTN4A-GFP under control conditions (left) or treated with nocodazole for 4 h (right).

(G–I) Representative still images of live DIV4 neurons expressing RTN4A-GFP and recorded during nocodazole treatment for 60 min (G) and 240 min (H) or Taxol treatment for 240 min (I). Kymographs of straightened regions from a dendrite in (G) (dashed cyan line) and from axons in (G) and (H) (magenta dashed lines) are shown on the left. Also shown is the average RTN4A intensity of a dendrite (cyan) and proximal axon (magenta) over the time of Taxol treatment (I).

Green and red arrowheads point to axonal ER or axonal Ac-Tub distribution, respectively, in (A)–(D). Cyan and magenta arrows points to dendrites and proximal axons, respectively, in (A)–(D) and (G)–(I). Scale bars represent 20 μm in (A), (B), (D), and (G)–(I); 5 μm in (F); and 2 μm in (C). See also Figure S4 and Video S3.

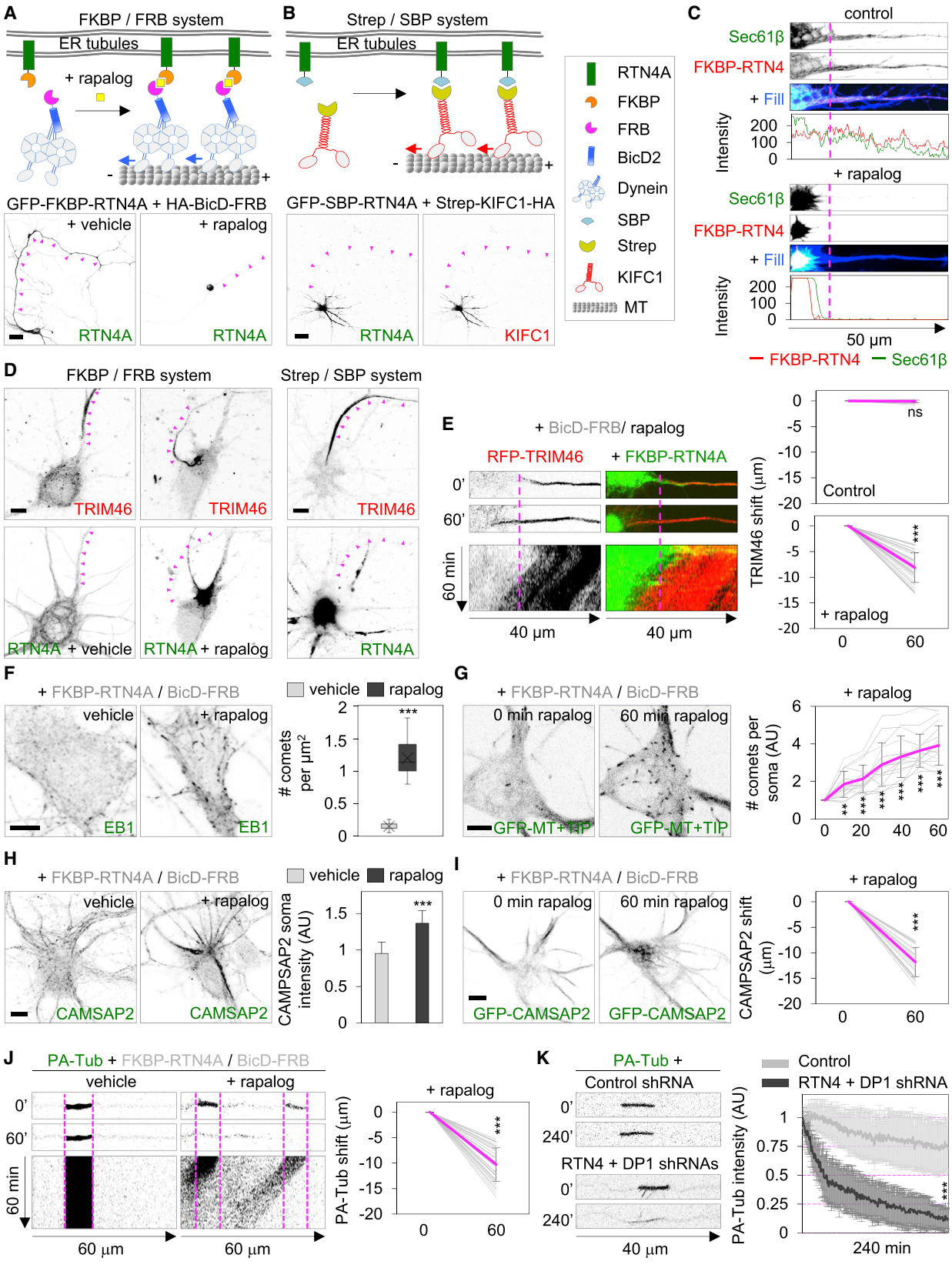

(legend on next page)

typically decorates MT stretches in the soma and proximal segments of dendrites and axons (Yau et al., 2014). ER tubule retraction caused a drastic shift of CAMSAP2 with stretches emanating from the perinuclear area (Figures 4H and 4I; Video S5B). To determine whether removal of ER tubules from the axon altered MT stability in the axon, we analyzed the dynamics of a photo-activatable GFP-α-tubulin (PA-Tub) construct. Photo-activated patches of PA-Tub in the axon of control neurons display a remarkable stable pool of MTs that last for several hours. However, ER tubule removal from the axon caused a retrograde flow of photoactivated tubulin patches in the axon, indicating that MTs became more dynamic after 1 h of rapalog treatment (Figure 4J; Video S6). Because shRNAs targeting RTN4 and DP1 also caused a reduction in axonal ER (Figures 2F and 2G), we wondered how PA-Tub behaves in axons from neurons knocked down for these proteins. PA-Tub was slightly displaced in the first hour and became substantially more dynamic after 4 h of recording in neurons expressing shRNAs for RTN4 plus DP1 compared with control neurons (Figure 4K). Because the role of MTs in the recruitment of axon initial segment (AIS) protein complex to the plasma membrane in the proximal axon (Fréal et al., 2016), we also analyzed the distribution and dynamics of AIS proteins in neurons depleted from axonal ER tubules. Ankyrin-G (AnkG), the master AIS organizer, as well as the interacting proteins NF, Na_V, and β_{IV}-Spectrin, were all disassembled from the proximal axon (Figure S6; Video S4B). Together, these results reveal a key role for ER tubules in the organization and dynamics of axonal MTs and in the assembly of the AIS.

Local Recruitment of ER Tubules to One Neurite Is Required for Axon Specification

MT stabilization by Taxol induces multiple axons in already polarized neurons (Gomis-Rüth et al., 2008). We analyzed how disruption of ER tubule formation affects the ability of Taxol to induce multiple axons in neurons at DIV7. Control-transfected neurons treated with Taxol for 72 h caused an ~4-fold increase in the number of axons positive for TRIM46 and AnkG markers (Figures 5A and 5B). In contrast, neurons knocked down for RTN4 and DP1 and treated with Taxol did not exhibit multiple axons and were similar to neurons treated with just vehicle (Figures 5A and 5B).

Increased MT stability as well as TRIM46 recruitment to a single neurite have been observed even before axon formation in neurons in the transition between stages 2 and 3 (Witte et al., 2008; van Beuningen et al., 2015). We analyzed the distribution of ER tubules in DIV1 neurons in which a mixed population of unpolarized neurons (stage 2) and axon-specified neurons positive for Tau (stage 3) can be observed. Interestingly, we found a population of unpolarized neurons in the transition of stage 2–3 that showed preferential distribution of endogenous RTN4 in one minor neurite that coincided with slightly more stable acetylated, detyrosinated MTs and that was also positive for TRIM46 (Figures 5C–5E). Moreover, we analyzed the dynamics of recruitment of RTN4A-GFP and RFP-TRIM46 in neurons during axon specification. Increased and persistent RTN4A transport to a minor neurite and recruitment of TRIM46 to the same neurite preceded axon specification (Figure 5F; Video S7A). TRIM46 was retained in the proximal part of the axon, but RTN4A

Figure 4. ER Tubules Regulate MT Organization in Neurons

(A) Schematic representation of the dynein complex targeting ER tubules for rapalog-induced MT-dependent retrograde transport from the axon to the soma using the FKBP-FRB rapalog-induced heterodimerization system (top). Also shown are representative images of the distribution of GFP-FKBP-RTN4A in DIV7 neurons co-transfected with HA-BicD2-FRB and treated with 100 nM rapalog for 1 h (right) or just vehicle (0.1% ethanol, left) (bottom).

(B) Schematic representation of the minus end-driven KIFC1 motor targeting ER tubules for MT-dependent retrograde transport and persistent retention in the somatodendritic domain using the Streptavidin (Strep)-SBP heterodimerization system. Also shown is a representative image of the distribution of GFP-SBP-RTN4A (left) and Strep-KIFC1-HA (right) in DIV7 neurons transfected on DIV6 (bottom).

(C) Soma-axon straightened regions of DIV7 neurons expressing mCh-FKBP-RTN4A (red), HA-BicD-FRB, or fill (blue) plus GFP-Sec61β (green) in control or rapalog-treated cells. Also shown are diagrams corresponding to the average fluorescence intensity profiles of each condition (bottom).

(D) Representative images of neurons transfected and treated as in (A) or just transfected as in (B) and stained for endogenous TRIM46 (top). GFP-FKBP-RTN4A or GFP-SBP-RTN4A are shown at the bottom.

(E) Representative still images and kymograph from a straightened soma-axon region of a live neuron transfected with GFP-FKBP-RTN4A (green) and HA-BicD2-FRB and RFP-TRIM46 (red), recorded in the presence of rapalog for 1 h. See also Video S4A. Quantification of the TRIM46 shift in several control and rapalog-treated neurons is shown on the right. n = 25 and 35 neurons, respectively (paired t test).

(F) Representative images of neurons co-transfected with mCh-FKBP-RTN4A plus BicD2-FRB, treated with rapalog or vehicle for 1 h, and stained for endogenous EB1. Quantification corresponds to the number of EB1 comets per square μm. n = 24 neurons per condition (unpaired t test).

(G) Representative still images of a live neuron transfected as in (F) plus GFP-MT-TIP, recorded in the presence of rapalog for 60 min. Quantification corresponds to the number of MT+TIP comets per square μm. n = 16 neurons (one-way ANOVA followed by Dunnett's multiple comparisons test).

(H) Representative images of neurons transfected and treated as in (F), stained for endogenous CAMSAP2, and the corresponding quantification of CAMSAP2 intensity at the soma. n = 29 neurons per condition (unpaired t test).

(I) Representatives still images of a live neuron transfected as in (F) plus GFP-CAMSAP2, recorded in the presence of rapalog for 60 min. Quantification corresponds to the CAMSAP2 shift from proximal neurites to the perinuclear area in μm during the 60-min rapalog treatment. n = 23 neurons (Wilcoxon signed-rank test).

(J) Representatives still images and kymographs of straightened axons from DIV6 live neurons transfected as in (F) plus PA-GFP-α-tubulin (PA-Tub). Photoactivation of PA-Tub was performed prior to live-cell imaging in the presence of rapalog or vehicle for 1 h. Quantification correspond to the PA-Tub shift in μm. n = 34 neurons per condition (Wilcoxon signed-rank test).

(K) Representative still images of straightened axons from DIV6 neurons transfected with PA-Tub plus control pSuper vector or shRNAs for RTN4A and DP1 and quantification of PA-Tub intensity post-photoactivation decay in neurons live-cell-recorded for 4 h. n = 10–12 neurons per condition.

Scale bars represent 20 μm in (A) and (B) and 5 μm in (D) and (F)–(I). The graphs in (F), (H), and (K) shown the mean ± SD. The graphs in (E), (G), (I), and (J) show quantification in several neurons, and the mean ± SD is shown in magenta. ***$p < 0.001$, comparing individual conditions with the control. See also Figures S4E and S5 and Videos S4, S5, and S6.

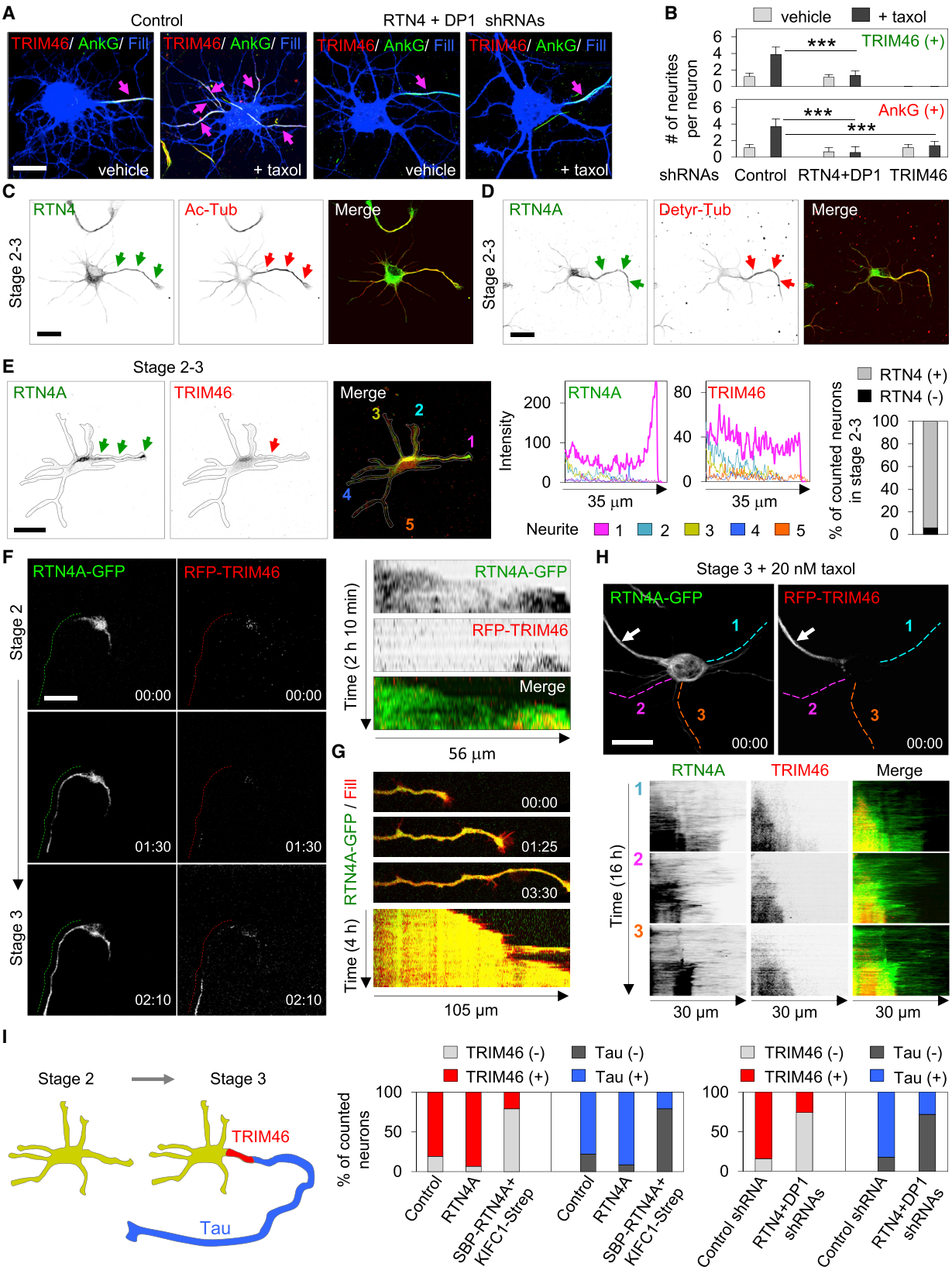

(legend on next page)

continued to slide along the entire axon during axon elongation (Figure 5G; Video S7B). To corroborate these results, we also treated neurons at stage 3 with Taxol to induce multiple axons and evaluate the recruitment of RTN4A-GFP and RFP-TRIM46 to the new axons in formation by live-cell imaging. Before adding Taxol to neurons, RTN4A and TRIM46 were mostly distributed in the formed axon, but after hours of treatment, both proteins were also targeted to other neurites prior to their elongation and specification of the new axons (Figure 5H; Video S7C).

Importantly, we analyzed whether the recruitment of ER tubules to a minor neurite was required for the specification of the axon. We utilized the Streptavidin-SBP system (Figure 4B) to produce immediate and sustained retention of ER tubules at the soma. Neurons were nucleofected in suspension prior plating on DIV0, and the percentages of neurons in stages 2 and 3 were quantified at DIV2 based on positive staining for endogenous TRIM46 and Tau and axon length (Figure 5I). ER tubule retention caused a reduction of neurons in stage 3, as determined by an increased population of neurons negative for TRIM46 and Tau staining as well as an increased number of neurons with only short minor neurites (Figure 5I; Figure S7A). Disruption of ER tubule formation by expressing shRNAs for RTN4 and DP1 produced similar results (Figure 5I; Figure S7B). We also examined whether ER tubules play a role during neuron polarization and migration *in situ*. Mouse brains were electroporated *ex vivo* at embryonic day 14.5 (E14.5) with control and RTN4 plus DP1 shRNAs together with GFP to visualize neuronal morphology. After 4 days, control neurons efficiently migrated to the upper layers of the cortical plate and developed a typical bipolar morphology with a trailing edge (future axon) and leading process (future apical dendrite). In contrast, ER tubule-depleted neurons failed to migrate properly and accumulated in the ventricular and subventricular zones (Figures S7D and S7E). Thus, the distribution of ER tubules in neurites is required for the specification of the axon and neuron migration.

P180 Distributes in a Particular Set of ER Tubules in the Axon but Not Dendrites to Regulate Axonal ER Distribution

We next investigated the mechanism by which ER tubules control ER-MT co-stabilization and neuronal polarity. Among all of the ER-shaping proteins described, only CLIMP63, P180, and REEP1 have been shown to directly interact with and bundle MTs in non-neuronal cells (Klopfenstein et al., 1998; Ogawa-Goto et al., 2007; Park et al., 2010). In neurons, CLIMP63 distributed in the somatodendritic domain, REEP1 has been shown previously to distribute mainly in axonal branches and axonal tips (Park et al., 2010), and P180 localization has not yet been studied. Mass spectrometry analysis indicated that P180 was expressed in our primary culture of neurons (Figure S3C). Therefore, we analyzed and compared the distribution of P180 in COS-7 cells and cultured neurons. In COS-7 cells, GFP-tagged P180 was distributed in perinuclear ER cisternae (Figures 6A and 6I), as reported previously (Ogawa-Goto et al., 2007). Interestingly, in neurons, the distribution was slightly different. GFP-P180 was localized in ER cisternae at the soma but also present in ER tubule-like structures distributed mainly in the axon and excluded from dendrites (PI, ~ -0.9; Figures 6B–6D). P180 was particularly abundant in the more proximal segment of the axon (Figure 6E). Knockdown of the ER tubule-shaping proteins RTN4 and DP1 as well as overexpression of CLIMP63 caused exclusion of GFP-P180 from the axon and its main distribution in the soma as ER cisternae, which confirmed the nature of these axonal ER membranes containing P180 as ER tubules (Figures 6F and 6G).

P180 contains a short luminal and single-transmembrane domain followed by a long cytosolic tail featuring the presence of a basic decapeptide repeat and an acidic coiled-coil (CC) domain. To identify the domains responsible for the distribution of P180 within the ER, we generated various P180 deletion constructs (Figure 6H) and analyzed their distribution in COS-7 cells and in neurons. P180-Δcytosolic tail was distributed along all the

Figure 5. Targeting of ER Tubules to a Minor Neurite Is Required for Axon Specification

(A and B) Representative images of DIV7 neurons transfected with a plasmid containing shRNAs for RTN4 and DP1 or a control plasmid plus fill (blue), treated with 20 nM Taxol or vehicle for 72 h and stained for endogenous TRIM46 (green) and AnkG (red). Arrows point to axons (A). Quantification represents the number of neurites per neuron positive for TRIM46 (top) and AnkG (bottom) from the indicated conditions (B). A positive control of neurons expressing a plasmid containing shRNA for TRIM46 is included (B). n = 50 neurons per condition. In the graphs, mean ± SD is shown. ***p < 0.001 (Kruskal-Wallis test followed by Dunn's multiple comparisons test).

(C–E) Representative images of DIV1 neurons at stages 2–3 co-stained for endogenous RTN4 (green) and endogenous Ac-Tub (C) and detyrosinated tubulin (Detyr-Tub, D) and TRIM46 (E) (red). Arrows point to the distribution of both proteins in one minor neurite in (C)–(E). Diagrams show the average fluorescence intensity profiles for RTN4 (left) and TRIM46 (right) in minor neurites, indicated with numbers in the merged image in (E). Quantification in (E) represents the percentage of neurons at stages 2–3 (positive for TRIM46) that are positive or negative for RTN4A in the same minor neurite. n = 137 neurons.

(F) Representative still images and kymographs of a neuron nucleofected on DIV0 with RTN4A-GFP (green) and RFP-TRIM46 (red) and recorded from stage 2 to stage 3. Time is shown in hours:minutes. Dashed lines indicate the axon specification track.

(G) Representative still images and kymograph of a neuron nucleofected on DIV0 with RTN4A-GFP (green) and mCh (fill, red) and recorded during axon elongation. Time is shown in hours:minutes.

(H) Representative still images of a DIV3 neuron transfected as in (F) and treated with 20 nM Taxol and imaged for 16 h. Arrows point to the initial axon at time 0, and dashed lines 1, 2, and 3 correspond to the track for three dendrites that acquired RTN4 (green) and TRIM46 (red) during 16 h of Taxol treatment. Their respective kymographs are shown at the bottom.

(I) Schematic representation of neurons at stages 2 and 3 and quantification of axon specification. Neurons were nucleofected in suspension prior to plating with plasmids containing GFP-Sec61β (control), the ER tubule-shaping protein GFP-RTN4A, or the heterodimerization system to retain ER tubules in the perinuclear area (left graph). Also shown are control shRNA and RTN4 plus DP1 shRNAs (right graph). mCherry fill and staining for endogenous TRIM46 and Tau were used to identify neurons in stage 3 on DIV2 neurons. The numbers of counted neurons positive or negative for TRIM46 and Tau are expressed as percentages. n = 116–211 neurons per condition.

Scale bars represent 20 μm in all images. See also Figure S7 and Video S7.

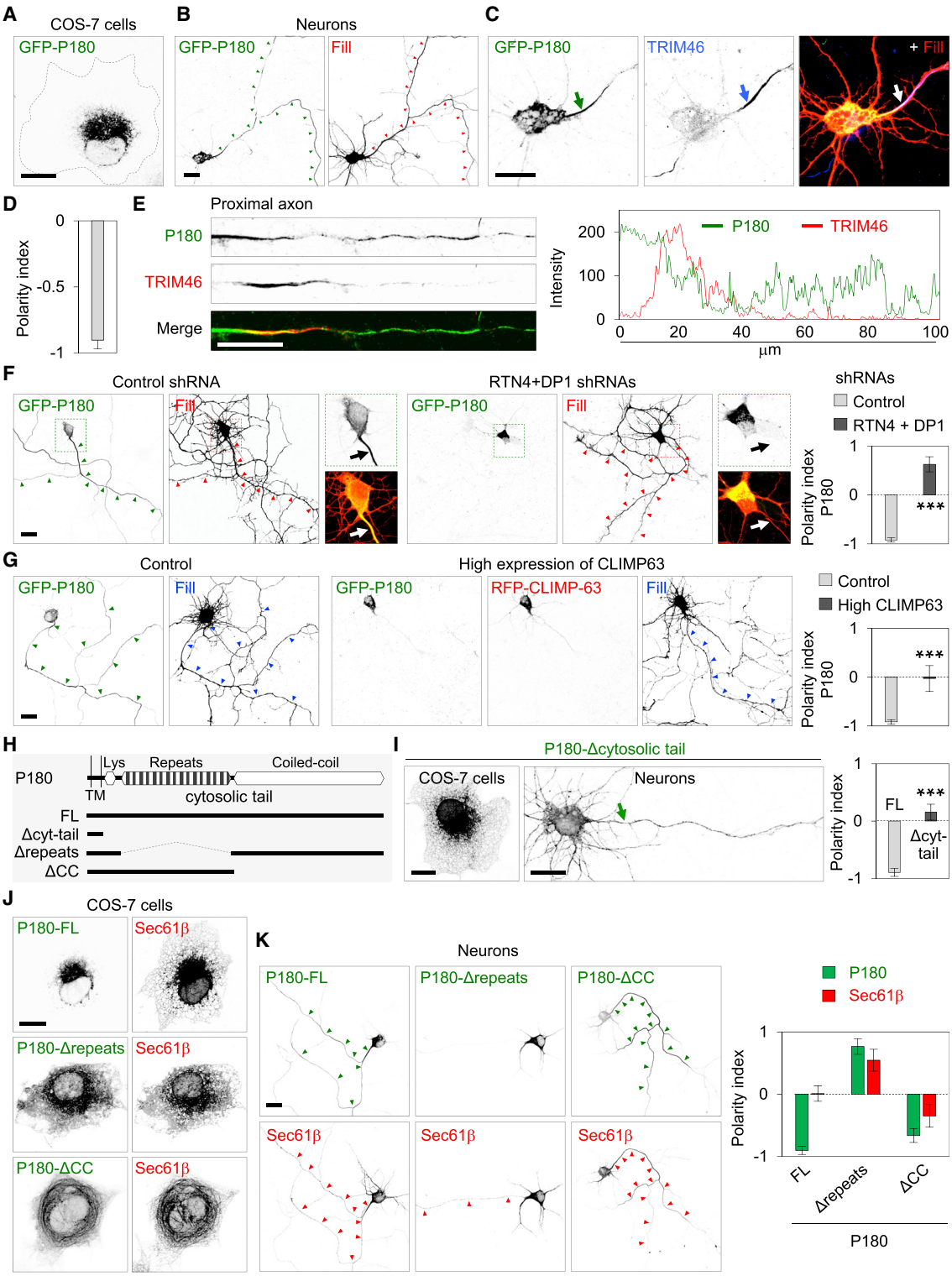

Figure 6. The ER-Resident Protein P180 Regulates the Shape and Distribution of the ER

(A) Representative image of a COS-7 cell transfected with GFP-P180.

(B and C) Representative images of a DIV7 neuron transfected with GFP-P180 (green) plus fill (red). The enlarged region of the images in (B) plus staining for endogenous TRIM46 are shown in (C).

(D) Polarity index for P180 in neurons transfected as in (B); n = 25 neurons.

(legend continued on next page)

ER, including ER tubules and ER cisternae in both types of cells, suggesting that the cytosolic tail is required for the preferential distribution of P180 in specific ER domains (Figure 6I). COS-7 cells and neurons expressing P180-Δrepeats or P180-ΔCC showed an ER cisterna and ER tubule distribution, respectively (Figures 6J and 6K). We also evaluated how the two domains of P180 contribute to the organization of the ER. Overexpression of P180-Δrepeats caused an expansion of ER cisternae and the disappearance of peripheral ER tubules in COS-7 cells, as evidenced by mCh-Sec61β distribution with respect to control cells expressing low levels of P180-full length (FL) (Figure 6J). Similar results were observed in neurons in which P180-Δrepeats and mCh-Sec61β were redistributed as ER cisternae in the somatodendritic domain (Figure 6K). On the other hand, expression of P180-ΔCC induced its co-distribution with mCh-Sec61β in highly curved ER structures in COS-7 cells, which were more abundant in the axon than in the somatodendritic domain of neurons (Figures 6J and 6K). These results indicate that two distinct regions of the cytosolic tail of P180 contribute to its distribution within the ER and confer to P180 the ability to regulate ER organization.

P180 Regulates MT Stabilization to Promote Axon Specification

Next, we analyzed how P180 contributes to MT stabilization. COS-7 cells expressing P180-ΔCC showed much higher levels of acetylated and bundled MTs than untransfected adjacent cells, which were aligned with the curved ER (Figures 7A–7C). The stabilization of MTs induced by P180-ΔCC was not observed by P180-Δrepeats and only slightly increased by P180-FL expression (Figure 7A). Accordingly, staining for EB1 showed a decrease in the number of comets in cells expressing P180-ΔCC, indicating less dynamics MTs (Figures 7D and 7E).

To determine the contribution of P180 to axonal MT stability, we analyzed the levels of acetylated α-tubulin in the axon. Neurons transfected with an shRNA targeting P180 showed a decrease in acetylated MTs compared with control neurons (Figure 7F). Moreover, analysis of photoactivated patches of PA-Tub in the axon of neurons knocked down for P180 showed more dynamic MTs compared with the static distribution of stable MTs 4 h after photoactivation (Figure 7G).

To investigate the link between MT stabilization mediated by P180 and axon specification, we used the Taxol treatment assay to induce multiple axons. P180 knockdown prevented Taxol-induced formation of multiple axons (Figure 7H). In contrast, we found that untreated neurons expressing just high levels of P180ΔCC induced the formation of multiple axons positive for TRIM46, which showed co-distribution of P180ΔCC with stabilized MTs (Figures 7I–7K). Finally, we analyzed the effect of P180 on axon specification. We nucleofected neurons in suspension with shRNA targeting P180 and stained for TRIM46 and Tau at DIV2. Knockdown of P180 decreased the percentage of neurons in stage 3 (Figure 7L; Figure S6C). Co-expression of a GFP-P180 shRNA-resistant construct was sufficient to rescue neuronal polarization (Figure 7L; Figure S7C). These results indicate that P180-induced MT stabilization facilitates axon specification.

DISCUSSION

Here we propose a feedback-driven model in which local interplay between the ER and MTs instructs neuronal polarity. MTs are required for the stabilization of ER tubules and their transport along the axon, and, concurrently, ER tubules are critically important for organizing axonal MTs. In unpolarized neurons, the formation of stable parallel MTs and the recruitment of ER tubules is essential to initiate axon formation. Our data suggest that the ER-shaping protein P180 acts as a positive regulator between the ER and MT cytoskeleton to control axon specification and neuronal polarity.

Segregation of ER Tubules and ER Cisternae in Neurons

ER membranes can form and maintain a stable reticular network by ER intrinsic mechanisms. A balance between ER cisterna- and ER tubule-shaping proteins as well as fusion between ER membranes regulates ER organization (Shibata et al., 2010; Wang et al., 2016). In this study, we found that the two different ER shapes, tubules and cisternae, are asymmetrically distributed in the axon and somatodendritic domain. Moreover, we found that overexpression of ER cisterna-shaping proteins as well knockdown of ER tubule shaping proteins caused a drastic reduction in axonal ER distribution. In the axon, long ER tubules interconnect with each other but do not show as much complexity as the reticular ER network observed in the somatodendritic domain (Wu et al., 2017). The thin diameter of the axon could be physically obstructing the formation of a wider ER network. However, the precise mechanism responsible for the distinct localization of ER tubules and ER cisternae remains

(E) Straightened 100-μm length of axon from the neuron in (B) and a diagram showing the average fluorescence intensity profiles for P180 (green) and TRIM46 (red).

(F) Representative images of neurons transfected with GFP-P180 (green) plus fill (red) together with the control pSuper plasmid or shRNAs for RTN4A plus DP1 and the polarity index for P180 from n = 25 neurons per condition.

(G) Representative images of neurons transfected with GFP-P180 (green) plus fill (red) in the presence or absence of high expression of CLIMP63 and the polarity index for P180 from n = 20 neurons per condition.

(H) Schematic representation of P180-FL domains and different deletion constructs.

(I) Representative images of a COS-7 cell (left) and DIV7 neuron (center) transfected with P180-Δcytosolic tail-GFP. Also shown is the polarity index for P180 from n = 20 neurons (right).

(J and K) Representative images of a COS-7 cell (J) and a DIV7 neuron (K) transfected with mCh-Sec61β and GFP-tagged P180-FL, P180-Δrepeats, or P180-Δcoiled-coil (CC) domains. Also shown are the polarity indexes for P180 and Sec61β from n = 20 neurons per condition (left).

Green arrowheads point to the axonal P180 in (B), (F), and (K). Red arrowheads point to the axonal Sec61β in (K), and red or blue arrowheads to the axonal domain in (B), (F), and (G). Arrows point to the proximal axon segment in (C), (F), and (I). Scale bars represent 20 μm in all images. In the graphs, mean ± SD is shown. ***$p < 0.001$ (t test) in (F)–(H).

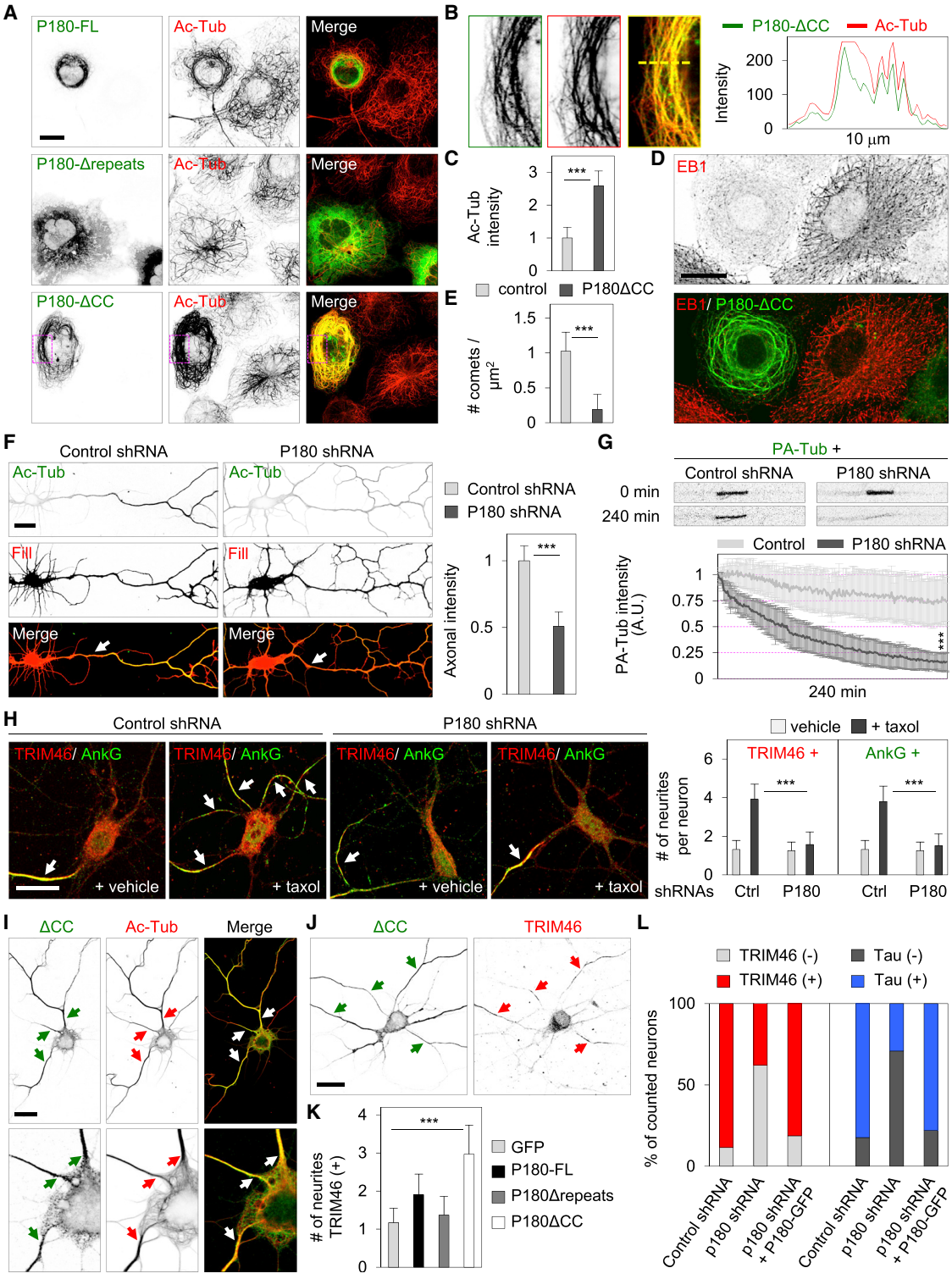

Figure 7. P180 Controls Axonal Specification by Regulating Microtubule Stability

(A) Representative images of COS-7 cells transfected with P180-FL, P180-Δrepeats, or P180-ΔCC (green) and stained for endogenous Ac-Tub (red).

(B and C) Enlarged region of a COS-7 cell from the dashed rectangle in (A). P180-ΔCC and Ac-Tub are shown in the images (left) and in the average fluorescence intensity profiles (right) as green and red, respectively (B). Also shown is quantification of the average intensity for Ac-Tub in cells expressing P180-ΔCC and in untransfected adjacent cells (control) (C). n = 40 cells per condition.

(legend continued on next page)

unclear. The AIS has been implicated in selective filtering of axonal and somatodendritic organelles (Leterrier, 2016). However, in developing neurons, ER cisternae were found in the somatodendritic domain but excluded from the axon before AIS establishment. Alternatively, association of ER tubule proteins with stable MTs may induce their stabilization and selective axonal transport, leaving ER cisternae behind in the somatodendritic compartment. On the other hand, other MAPs may retain ER cisternae in the somatodendritic domain. The polarized segregation of the two ER shapes in neurons is consistent with the distribution and organization of the biosynthetic pathway, where the rough ER (conformed by mainly ER cisterna membrane shape) produces and delivers transmembrane and secretion proteins to the Golgi complex, which is also located in the somatodendritic domain, to then sort these proteins into different set of vesicles for their polarized transport (Cui-Wang et al., 2012; Farías et al., 2015). Identifying the mechanism by which ER cisternae are excluded from the axon will be an important future research goal.

MT-Based Transport Distributes Axonal ER Tubules

ER tubules extend to the cell periphery by a tip attachment complex (TAC) mechanism in which ER tubules attach to growing plus ends of dynamic MTs through EBs (Grigoriev et al., 2008). Alternatively, sliding mechanisms have been reported, where ER tubules are transported along stable MTs (Waterman-Storer and Salmon; 1998; Friedman et al., 2010). In this study, we show that axonal ER tubules are transported by MT-based motors. We found that knockdown of KIF5 and dynein motors disrupted anterograde and retrograde ER tubule trafficking along the axon. The preferential association of KIF5 with stable axonal MTs may specify ER transport into the axon. Knockdown of EBs did not affect axonal ER but reduced ER in dendrites. It is possible that a sliding mechanism is required for axonal ER trafficking and that a TAC-based mechanism contributes to dendritic ER transport. Although ER-resident proteins involved in the sliding mechanism have not been identified, some studies suggest that the ER cisterna-shaping protein KTN1 could act as a receptor for KIF5 (Toyoshima et al., 1992; Kumar et al., 1995). Because of its exclusion from the axon, it is unlikely that KTN1 facilitates the sliding of ER tubules along axonal MTs. However, the ER-shaping protein P180 contains a KTN1 homologous region that can also bind KIF5 (Diefenbach et al., 2004). We found P180 distributed in both ER cisternae in the soma and ER tubules in the axon. Besides a KIF5 binding site, P180 contains two MT binding domains that are absent in KTN1 (Ogawa-Goto et al., 2007) and may help to stabilize ER tubules for proper KIF5-mediated axonal ER trafficking.

Interplay between ER Tubules and the MT Cytoskeleton during Neuronal Polarity

MT remodeling plays a critical role during neuronal polarization (Kapitein and Hoogenraad, 2015). The presence of stable and parallel MT arrays (van Beuningen et al., 2015) and the axonal distribution of ER tubules during the early steps of neuronal polarization led us to hypothesize that the interplay between ER and MTs induces changes in the cellular shape required for axon formation. Indeed, we found that local recruitment of ER tubules to a minor neurite preceded axon formation. On the other hand, axon outgrowth was inhibited by retention of ER tubules in the perinuclear area and disruption of ER tubules. Moreover, blocking ER tubule formation prevented the formation of multiple axons induced by Taxol. We propose a model in which the ER tubule-MT interplay drives neuronal polarity. This process starts with the formation of stable parallel MT arrays by specific axonal MAPs such as TRIM46. Concurrently, interaction between MTs and the newly formed ER tubule in one minor neurite may further stabilize this MT organization required for axon elongation. ER proteins that interact with MTs, such as P180, may act as cross-linkers between the ER and axonal MTs to co-stabilize and reinforce the ER tubule-MT interaction. Our data showed that pulling ER tubules to the perinuclear area induced the relocation of stable axonal MT bundles. Moreover, pulling ER tubules to the perinuclear area, ER tubule disruption, as well as P180 knockdown all caused axonal MT instability. Other ER tubule proteins may be involved in additional MT remodeling processes during later stages of axon outgrowth. For instance, the interaction of REEP1, ATL1, and the MT-severing protein spastin has been suggested to contribute to MT dynamics at axonal branchpoints and growth cones (Park et al., 2010). The presence of ER tubules in the newly formed axon may provide a local source of lipid

(D and E) Representative image of COS-7 cells transfected with P180-ΔCC (green) and stained for endogenous EB1 (red) (D). Also shown is quantification of the number of EB1 comets per square μm per cell in transfected versus untransfected adjacent cells (E). n = 40 cells per condition.
(F) Representative images of DIV4 neurons transfected on DIV2 with pSuper (control) or shRNA for P180 plus fill (red) and stained for endogenous Ac-Tub (green). Normalized axonal intensity of Ac-Tub in the first 150 μm of axon length is shown. n = 30 neurons per condition.
(G) Representative still images and quantification of PA-Tub dynamics post-photoactivation of axons from neurons transfected on DIV4 as in (F) plus PA-Tub and live-cell-recorded for 4 h on DIV6. In the graph, n = 11–14 per condition.
(H) Representative images of neurons transfected on DIV3 as in (F), treated with 20 nM Taxol or vehicle for 72 h and stained for endogenous TRIM46 (red) and AnkG (green) on DIV7. Quantification represents the number of neurites per neuron positive for TRIM46 and AnkG from the indicated conditions. n = 70 neurons per condition.
(I) Representative images of a DIV5 neuron transfected on DIV1 with P180-ΔCC (green) and stained for endogenous Ac-Tub (red). A higher magnification of the soma and proximal axon region is shown at the bottom.
(J and K) Representative images of a DIV7 neuron transfected on DIV3 with P180-ΔCC and stained for endogenous TRIM46 (J). Quantification corresponds to the number of neurites positive for TRIM46 of neurons transfected with the GFP-empty plasmid or GFP-tagged P180-FL, P180-Δrepeats, or P180-ΔCC. n = 60 neurons per condition (K).
(L) Quantification representing the percentage of neurons in stages 2 and 3 at DIV2. Neurons were nucleofected in suspension prior to plating with empty pSuper plasmid, shRNA for P180, or P180-shRNA plus shRNA-resistant P180-GFP (rescue). A fluorescent empty plasmid and staining for endogenous TRIM46 and Tau were used to identify transfected neurons in stage 3 on DIV2. n = 144–308 neurons per condition. See also Figure S7C.
Arrows point to the proximal axon segment in (F), (H)–(J). Scale bars represent 20 μm in all images. In the graphs, mean ± SD is shown. ***$p < 0.001$, comparing individual conditions with the control; unpaired t test in (C) and (E) and Kruskal-Wallis test followed by Dunn's multiple comparisons test in (H) and (K).

and/or control local calcium homeostasis. Both ER-related processes have been shown to be required for axon outgrowth and guidance (Posse de Chaves et al., 1995; Tojima, 2012). It will be important to investigate the precise role of ER tubules in axon formation and outgrowth in future studies.

In summary, our data demonstrate that the interplay between the ER and MT cytoskeleton is critical for axonal specification and neuronal polarity. We found that the interaction between ER-shaping proteins and axonal MTs is required for maintaining proper axonal architecture. Alterations in ER function and MT organization have been described in several neurodegenerative diseases (Franker and Hoogenraad, 2013; Goyal and Blackstone, 2013; Gurel et al., 2014). For instance, mutations in ER-resident proteins such ATL1 (SPG3A), REEP1 (SPG31), and RTN2 (SPG12) and MT-remodeling factors such as spastin (SPG4) cause spastic paraplegia, a syndrome characterized by progressive weakness and spasticity (stiffness) mainly caused by motor-sensory axon degeneration (Goyal and Blackstone, 2013), and loss of these hereditary spastic paraplegia (HSP) proteins lead to partial loss of the ER from distal axons as well as fewer but enlarged and occasionally discontinuous ER tubules in *Drosophila* larval peripheral nerve axons (Yalçın et al., 2017). In addition, amyotrophic lateral sclerosis (ALS)-linked mutations in the ER protein VAPB have been shown to disrupt ER organization (Fasana et al., 2010), and RTN4A overexpression prevents axon degeneration in another ALS mutant mouse model (Yang et al., 2009). Our current findings provide new molecular insights into how imbalance in ER-MT interactions could contribute to neurodegenerative diseases.

STAR★METHODS

Detailed methods are provided in the online version of this paper and include the following:

- KEY RESOURCES TABLE
- CONTACT FOR REAGENT AND RESOURCE SHARING
- EXPERIMENTAL MODEL AND SUBJECT DETAILS
  - Animals
  - Primary neuronal cultures and transfection
  - *Ex vivo* electroporation and organotypic brain slice cultures
  - Heterologous cell culture and transfection
- METHOD DETAILS
  - DNA and shRNA Constructs
  - Antibodies and reagents
  - Drug treatments
  - Mass spectrometry
  - Immunofluorescence staining and imaging
  - Live-cell imaging
  - Fluorescence recovery after photobleaching and photo-activation
  - Streptavidin/SBP heterodimerization system assay
  - Drug-induced FKBP/FRB heterodimerization system assay
  - Labeling of ER membrane in fixed and live neurons
  - Image analysis and quantification
- QUATIFICATION AND STATISTICAL ANALYSIS

SUPPLEMENTAL INFORMATION

Supplemental Information includes seven figures and seven videos and can be found with this article online at https://doi.org/10.1016/j.neuron.2019.01.030.

ACKNOWLEDGMENTS

We thank Dr. Juan Bonifacino for sharing the GFP-KIF5A-rigor construct. This work was supported by the Netherlands Organization for Scientific Research (NWO-ALW-VICI 865.10.010 to C.C.H.); the Foundation for Fundamental Research on Matter (FOM program 137; to C.C.H.), which is part of the NWO; the Netherlands Organization for Health Research and Development (ZonMW-TOP 912.16.058 to C.C.H.); the European Research Council (ERC) (ERC Consolidator 617050 to C.C.H.); and Alzheimer Nederland (WE. 15045 to C.C.H.).

AUTHOR CONTRIBUTIONS

G.G.F. designed and performed experiments, analyzed data, coordinated the study, and wrote the manuscript. A.F. performed electroporation at DIV0 for axon specification and mass spectrometry experiments. E.T. performed initial axon elongation experiments. R.S. performed mass spectrometry experiments. X.P. performed *ex vivo* image acquisition and quantification. S.P. and L.W. performed *ex vivo* electroporation and organotypic brain slice cultures. M.A. supervised mass spectrometry analysis. C.C.H. supervised the research, coordinated the study, and wrote the manuscript.

DECLARATION OF INTERESTS

The authors declare no competing interests.

Received: June 23, 2018
Revised: November 29, 2018
Accepted: January 15, 2019
Published: February 13, 2019

SUPPORTING CITATIONS

The following reference appears in the Supplemental Information: Frese et al. (2017).

REFERENCES

Baas, P.W., Rao, A.N., Matamoros, A.J., and Leo, L. (2016). Stability properties of neuronal microtubules. Cytoskeleton (Hoboken) *73*, 442–460.

Blackstone, C. (2012). Cellular pathways of hereditary spastic paraplegia. Annu. Rev. Neurosci. *35*, 25–47.

Brummelkamp, T.R., Bernards, R., and Agami, R. (2002). A system for stable expression of short interfering RNAs in mammalian cells. Science *296*, 550–553.

Conde, C., and Cáceres, A. (2009). Microtubule assembly, organization and dynamics in axons and dendrites. Nat. Rev. Neurosci. *10*, 319–332.

Cui-Wang, T., Hanus, C., Cui, T., Helton, T., Bourne, J., Watson, D., Harris, K.M., and Ehlers, M.D. (2012). Local zones of endoplasmic reticulum complexity confine cargo in neuronal dendrites. Cell *148*, 309–321.

De Paola, V., Arber, S., and Caroni, P. (2003). AMPA receptors regulate dynamic equilibrium of presynaptic terminals in mature hippocampal networks. Nat. Neurosci. *6*, 491–500.

Diefenbach, R.J., Diefenbach, E., Douglas, M.W., and Cunningham, A.L. (2004). The ribosome receptor, p180, interacts with kinesin heavy chain, KIF5B. Biochem. Biophys. Res. Commun. *319*, 987–992.

Dreier, L., and Rapoport, T.A. (2000). In vitro formation of the endoplasmic reticulum occurs independently of microtubules by a controlled fusion reaction. J. Cell Biol. *148*, 883–898.

Farías, G.G., Guardia, C.M., Britt, D.J., Guo, X., and Bonifacino, J.S. (2015). Sorting of dendritic and axonal vesicles at the pre-axonal exclusion zone. Cell Rep. *13*, 1221–1232.

Farías, G.G., Guardia, C.M., De Pace, R., Britt, D.J., and Bonifacino, J.S. (2017). BORC/kinesin-1 ensemble drives polarized transport of lysosomes into the axon. Proc. Natl. Acad. Sci. USA *114*, E2955–E2964.

Fasana, E., Fossati, M., Ruggiano, A., Brambillasca, S., Hoogenraad, C.C., Navone, F., Francolini, M., and Borgese, N. (2010). A VAPB mutant linked to amyotrophic lateral sclerosis generates a novel form of organized smooth endoplasmic reticulum. FASEB J. *24*, 1419–1430.

Franker, M.A., and Hoogenraad, C.C. (2013). Microtubule-based transport - basic mechanisms, traffic rules and role in neurological pathogenesis. J. Cell Sci. *126*, 2319–2329.

Fréal, A., Fassier, C., Le Bras, B., Bullier, E., De Gois, S., Hazan, J., Hoogenraad, C.C., and Couraud, F. (2016). Cooperative interactions between 480 kDa Ankyrin-G and EB proteins assemble the axon initial segment. J. Neurosci. *36*, 4421–4433.

Frese, C.K., Mikhaylova, M., Stucchi, R., Gautier, V., Liu, Q., Mohammed, S., Heck, A.J.R., Altelaar, A.F.M., and Hoogenraad, C.C. (2017). Quantitative map of proteome dynamics during neuronal differentiation. Cell Rep. *18*, 1527–1542.

Friedman, J.R., Webster, B.M., Mastronarde, D.N., Verhey, K.J., and Voeltz, G.K. (2010). ER sliding dynamics and ER-mitochondrial contacts occur on acetylated microtubules. J. Cell Biol. *190*, 363–375.

Gomis-Rüth, S., Wierenga, C.J., and Bradke, F. (2008). Plasticity of polarization: changing dendrites into axons in neurons integrated in neuronal circuits. Curr. Biol. *18*, 992–1000.

Goyal, U., and Blackstone, C. (2013). Untangling the web: mechanisms underlying ER network formation. Biochim. Biophys. Acta *1833*, 2492–2498.

Grigoriev, I., Gouveia, S.M., van der Vaart, B., Demmers, J., Smyth, J.T., Honnappa, S., Splinter, D., Steinmetz, M.O., Putney, J.W., Jr., Hoogenraad, C.C., and Akhmanova, A. (2008). STIM1 is a MT-plus-end-tracking protein involved in remodeling of the ER. Curr. Biol. *18*, 177–182.

Gurel, P.S., Hatch, A.L., and Higgs, H.N. (2014). Connecting the cytoskeleton to the endoplasmic reticulum and Golgi. Curr. Biol. *24*, R660–R672.

Honnappa, S., Gouveia, S.M., Weisbrich, A., Damberger, F.F., Bhavesh, N.S., Jawhari, H., Grigoriev, I., van Rijssel, F.J., Buey, R.M., Lawera, A., et al. (2009). An EB1-binding motif acts as a microtubule tip localization signal. Cell *138*, 366–376.

Hung, V., Lam, S.S., Udeshi, N.D., Svinkina, T., Guzman, G., Mootha, V.K., Carr, S.A., and Ting, A.Y. (2017). Proteomic mapping of cytosol-facing outer mitochondrial and ER membranes in living human cells by proximity biotinylation. eLife *6*, e24463.

Jaworski, J., Kapitein, L.C., Gouveia, S.M., Dortland, B.R., Wulf, P.S., Grigoriev, I., Camera, P., Spangler, S.A., Di Stefano, P., Demmers, J., et al. (2009). Dynamic microtubules regulate dendritic spine morphology and synaptic plasticity. Neuron *61*, 85–100.

Kapitein, L.C., and Hoogenraad, C.C. (2015). Building the neuronal microtubule cytoskeleton. Neuron *87*, 492–506.

Kapitein, L.C., Schlager, M.A., van der Zwan, W.A., Wulf, P.S., Keijzer, N., and Hoogenraad, C.C. (2010). Probing intracellular motor protein activity using an inducible cargo trafficking assay. Biophys. J. *99*, 2143–2152.

Klopfenstein, D.R., Kappeler, F., and Hauri, H.P. (1998). A novel direct interaction of endoplasmic reticulum with microtubules. EMBO J. *17*, 6168–6177.

Komarova, Y., Lansbergen, G., Galjart, N., Grosveld, F., Borisy, G.G., and Akhmanova, A. (2005). EB1 and EB3 control CLIP dissociation from the ends of growing microtubules. Mol. Biol. Cell *16*, 5334–5345.

Kononenko, N.L., Claßen, G.A., Kuijpers, M., Puchkov, D., Maritzen, T., Tempes, A., Malik, A.R., Skalecka, A., Bera, S., Jaworski, J., and Haucke, V. (2017). Retrograde transport of TrkB-containing autophagosomes via the adaptor AP-2 mediates neuronal complexity and prevents neurodegeneration. Nat. Commun. *8*, 14819.

Kuijpers, M., van de Willige, D., Freal, A., Chazeau, A., Franker, M.A., Hofenk, J., Rodrigues, R.J., Kapitein, L.C., Akhmanova, A., Jaarsma, D., and Hoogenraad, C.C. (2016). Dynein regulator NDEL1 controls polarized cargo transport at the axon initial segment. Neuron *89*, 461–471.

Kumar, J., Yu, H., and Sheetz, M.P. (1995). Kinectin, an essential anchor for kinesin-driven vesicle motility. Science *267*, 1834–1837.

Leterrier, C. (2016). The axon initial segment, 50 years later: a nexus for neuronal organization and function. Curr. Top. Membr. *77*, 185–233.

Nikonov, A.V., Hauri, H.P., Lauring, B., and Kreibich, G. (2007). Climp-63-mediated binding of microtubules to the ER affects the lateral mobility of translocon complexes. J. Cell Sci. *120*, 2248–2258.

Nixon-Abell, J., Obara, C.J., Weigel, A.V., Li, D., Legant, W.R., Xu, C.S., Pasolli, H.A., Harvey, K., Hess, H.F., Betzig, E., et al. (2016). Increased spatiotemporal resolution reveals highly dynamic dense tubular matrices in the peripheral ER. Science *354*, aaf3928.

Ogawa-Goto, K., Tanaka, K., Ueno, T., Tanaka, K., Kurata, T., Sata, T., and Irie, S. (2007). p180 is involved in the interaction between the endoplasmic reticulum and microtubules through a novel microtubule-binding and bundling domain. Mol. Biol. Cell *18*, 3741–3751.

Park, S.H., Zhu, P.P., Parker, R.L., and Blackstone, C. (2010). Hereditary spastic paraplegia proteins REEP1, spastin, and atlastin-1 coordinate microtubule interactions with the tubular ER network. J. Clin. Invest. *120*, 1097–1110.

Posse de Chaves, E., Vance, D.E., Campenot, R.B., and Vance, J.E. (1995). Axonal synthesis of phosphatidylcholine is required for normal axonal growth in rat sympathetic neurons. J. Cell Biol. *128*, 913–918.

Shibata, Y., Voeltz, G.K., and Rapoport, T.A. (2006). Rough sheets and smooth tubules. Cell *126*, 435–439.

Shibata, Y., Voss, C., Rist, J.M., Hu, J., Rapoport, T.A., Prinz, W.A., and Voeltz, G.K. (2008). The reticulon and DP1/Yop1p proteins form immobile oligomers in the tubular endoplasmic reticulum. J. Biol. Chem. *283*, 18892–18904.

Shibata, Y., Shemesh, T., Prinz, W.A., Palazzo, A.F., Kozlov, M.M., and Rapoport, T.A. (2010). Mechanisms determining the morphology of the peripheral ER. Cell *143*, 774–788.

Terasaki, M., Chen, L.B., and Fujiwara, K. (1986). Microtubules and the endoplasmic reticulum are highly interdependent structures. J. Cell Biol. *103*, 1557–1568.

Tojima, T. (2012). Intracellular signaling and membrane trafficking control bidirectional growth cone guidance. Neurosci. Res. *73*, 269–274.

Toyoshima, I., Yu, H., Steuer, E.R., and Sheetz, M.P. (1992). Kinectin, a major kinesin-binding protein on ER. J. Cell Biol. *118*, 1121–1131.

van Beuningen, S.F.B., Will, L., Harterink, M., Chazeau, A., van Battum, E.Y., Frias, C.P., Franker, M.A.M., Katrukha, E.A., Stucchi, R., Vocking, K., et al. (2015). TRIM46 controls neuronal polarity and axon specification by driving the formation of parallel microtubule arrays. Neuron *88*, 1208–1226.

Voeltz, G.K., Prinz, W.A., Shibata, Y., Rist, J.M., and Rapoport, T.A. (2006). A class of membrane proteins shaping the tubular endoplasmic reticulum. Cell *124*, 573–586.

Wang, S., Tukachinsky, H., Romano, F.B., and Rapoport, T.A. (2016). Cooperation of the ER-shaping proteins atlastin, lunapark, and reticulons to generate a tubular membrane network. eLife *5*, e18605.

Waterman-Storer, C.M., and Salmon, E.D. (1998). Endoplasmic reticulum membrane tubules are distributed by microtubules in living cells using three distinct mechanisms. Curr. Biol. *8*, 798–806.

Witte, H., Neukirchen, D., and Bradke, F. (2008). Microtubule stabilization specifies initial neuronal polarization. J. Cell Biol. *180*, 619–632.

Woźniak, M.J., Bola, B., Brownhill, K., Yang, Y.C., Levakova, V., and Allan, V.J. (2009). Role of kinesin-1 and cytoplasmic dynein in endoplasmic reticulum movement in VERO cells. J. Cell Sci. *122*, 1979–1989.

Wu, Y., Whiteus, C., Xu, C.S., Hayworth, K.J., Weinberg, R.J., Hess, H.F., and De Camilli, P. (2017). Contacts between the endoplasmic reticulum and other membranes in neurons. Proc. Natl. Acad. Sci. USA *114*, E4859–E4867.

Yalçın, B., Zhao, L., Stofanko, M., O'Sullivan, N.C., Kang, Z.H., Roost, A., Thomas, M.R., Zaessinger, S., Blard, O., Patto, A.L., et al. (2017). Modeling of axonal endoplasmic reticulum network by spastic paraplegia proteins. eLife *6*, e23882.

Yang, Y.S., Harel, N.Y., and Strittmatter, S.M. (2009). Reticulon-4A (Nogo-A) redistributes protein disulfide isomerase to protect mice from SOD1-dependent amyotrophic lateral sclerosis. J. Neurosci. *29*, 13850–13859.

Yau, K.W., van Beuningen, S.F., Cunha-Ferreira, I., Cloin, B.M., van Battum, E.Y., Will, L., Schätzle, P., Tas, R.P., van Krugten, J., Katrukha, E.A., et al. (2014). Microtubule minus-end binding protein CAMSAP2 controls axon specification and dendrite development. Neuron *82*, 1058–1073.

Zhu, Y., Zhang, G., Lin, S., Shi, J., Zhang, H., and Hu, J. (2018). Sec61β facilitates the maintenance of endoplasmic reticulum homeostasis by associating microtubules. Protein Cell *9*, 616–628.

STAR★METHODS

KEY RESOURCES TABLE

REAGENT or RESOURCE	SOURCE	IDENTIFIER
Antibodies		
Rabbit anti-RTN4 (named Nogo)	Novus	NB100-56681: RRID: AB_838641
Mouse anti-RTN4A (named NogoA)	R&D Systems	MAB3098; RRID: AB_10997139
Mouse anti-KDEL (clone 10C3)	Stressgen/Enzo	SPA-827; RRID: AB_10618036
Mouse anti-Tau (clone PC1C6)	Chemicon	MAB3420; RRID: AB_94855
Chicken anti-MAP2	Abcam	ab5392; RRID: AB_2138153
Rabbit anti-TRIM46	From Dr. Casper Hoogenraad, van Beuningen et al., 2015	N/A
Mouse anti-AnkG (clone N106/36)	UC Davis/NIH NeuroMab	75-146; RRID: AB_10673030
Mouse anti-Pan-Neurofascin (external; clone A12/18)	UC Davis/NIH NeuroMab	75-172; RRID: AB_2282826
Mouse anti-Sodium channel (Pan, clone K58/35)	Sigma-Aldrich	S8809; RRID: AB_477552
Rabbit anti βIV-Spectrin	Kind gift from Dr. Matthew Rasband	N/A
Mouse anti-acetylated tubulin	Sigma-Aldrich	T7451; RRID: AB_609894
Rabbit anti-detyrosinated tubulin	Millipore	AB3201; RRID: AB_177350
Mouse anti-EB1 (clone 5/EB1)	BD Transduction Laboratories	610535; RRID: AB_397892
Rabbit anti-CAMSAP2	Proteintech	17880-1-AP; RRID: AB_2068826
Rabbit anti-GFP	Abcam	ab290; RRID: AB_303395
Rabbit anti-GFP	MBL International	598S; RRID: AB_591816
Mouse anti-GFP (3E6)	Thermo Fisher Scientific	A-11120; RRID: AB_221568
Mouse anti mCh	Clontech Laboratories	632543; RRID: AB_2307319
Mouse anti-HA (12CA5)	Roche	11666606001; RRID: AB_514506
Donkey anti-mouse Alexa488	Molecular Probes	A21202; RRID: AB_141607
Donkey anti-mouse Alexa555	Molecular Probes	A31570; RRID: AB_2536180
Donkey anti-mouse Alexa647	Molecular Probes	A31571; RRID: AB_162542
Donkey anti-rabbit Alexa488	Molecular Probes	A21206; RRID: AB_141708
Donkey anti-rabbit Alexa555	Molecular Probes	A31572; RRID: AB_162543
Donkey anti-rabbit Alexa647	Molecular Probes	A31573; RRID: AB_2536183
Goat anti-chicken Alexa647	Molecular Probes	A21449; RRID: AB_2535866
Goat anti-mouse Alexa405	Molecular Probes	A31553; RRID: AB_221604
Goat anti-rabbit Alexa405	Molecular Probes	A31556; RRID: AB_221605
Chemicals, Peptides, and Recombinant Proteins		
Paclitaxel (Taxol)	Sigma-Aldrich	T7402
Nocodazole	Sigma-Aldrich	M1404
Rapalog	Takara	635057
Neutravidin	Thermo-Fisher Scientific	31000
Lipofectamine 2000	Invitrogen	1639722
DiOC6(3) (3,3′-Dihexyloxacarbocyanine Iodide)	Thermo-Fisher Scientific	D273
ER-Tracker Red (BODIPY TR Glibenclamide)	Thermo-Fisher Scientific	E34250
Mix-n-Stain CF640R	Biotium	92245
FastGreen FCF Dye	Sigma	F7252
Critical Commercial Assays		
Rat Neuron Nucleofector kit	Amaxa	VVPG-1003
Deposited Data		
Raw mass-spectrometry data	This paper	PXD012264

(*Continued on next page*)

Continued

REAGENT or RESOURCE	SOURCE	IDENTIFIER
Experimental Models: Cell Lines		
African Green Monkey SV40-transformed kidney fibroblast (COS-7)	ATCC	CRL-1651
Experimental Models: Organisms/Strains		
Rat (Wistart)	Janvier	N/A
Mouse (C57Bl/6)	Janvier	N/A
Recombinant DNA		
RTN4A-GFP	Kind gift from Dr. Gia Voeltz; Shibata et al., 2008	Addgene; plasmid #61807
GFP-FKBP2X-RTN4A	This study	N/A
mCh-FKBP2X-RTN4A	This study	N/A
GFP-SBP-RTN4A	This study	N/A
mCh-SBP-RTN4A (named mCh-RTN4A)	This study	N/A
DP1-GFP	This study	N/A
GFP-ATL1	Kind gift from Dr. Tom Rapoport; Wang et al., 2016	Addgene; plasmid # 86679
RFP-CLIMP63	Kind gift from Dr. Tom Rapoport	N/A
GFP-KTN1	This study	N/A
GFP-Sec61β	Kind gift from Dr. Tom Rapoport	Addgene; plasmid # 15108
mCh-SBP-Sec61β (named mCh-Sec61β)	This study	N/A
HA-BicD2-FRB	Kind gift from Dr. Lukas Kapitein; Kapitein et al., 2010	N/A
Strep-KIFC1-HA	This study	N/A
GFP-P180 (GFP-RRBP1)	Kind gift from Dr. Alice Ting; Hung et al., 2017	Addgene; plasmid # 92150
P180Δcytosolic tail-GFP	This study	N/A
P180Δrepeats-GFP	This study	N/A
P180ΔCC-GFP	This study	N/A
RFP-TRIM46	van Beuningen et al., 2015	N/A
BFP-TRIM46	From C.C.H., unpublished data	N/A
AnkG480-GFP	Fréal et al., 2016	N/A
GFP-MT+TIP (GFP-MACF43)	Honnappa et al., 2009	N/A
GFP-CAMSAP2	Yau et al., 2014	N/A
PA-GFP-α-Tubulin	Kuijpers et al., 2016	N/A
GFP-KIF5A-Rigor (G235A)	Kind gift from Dr. Juan Bonifacino; Farías et al., 2015	N/A
pEGFP(A206K)-N1	Kind gift from Dr. Jennifer Lippincott-Schwartz	N/A
pEGFP(A206K)-C1	Kind gift from Dr. Jennifer Lippincott-Schwartz	N/A
pmCherry-N1	Clontech	632523
pmCherry-C1	Clontech	632524
pGW1-BFP	Kapitein et al., 2010	N/A
pGFP(A206)-SBP-C1	This study	N/A
mCh-SBP-C1	This study	N/A
MARCKS-GFP	De Paola et al., 2003	N/A
pSuper vector	Brummelkamp et al., 2002	N/A
pSuper-rat KIF5A; shRNA targeting sequence gagacatcttcaaccacat	From C.C.H., unpublished data	N/A

(*Continued on next page*)

Continued

REAGENT or RESOURCE	SOURCE	IDENTIFIER
pSuper-rat KIF5B; shRNA targeting sequence tggagggtaaacttcatga	From C.C.H., unpublished data	N/A
pSuper-rat KIF5C; shRNA targeting sequence tgagatctacttggacaaa	From C.C.H., unpublished data	N/A
pSuper-rat KIF1A; shRNA targeting sequence cacgccgtcttcaacatca	From C.C.H., unpublished data	N/A
pSuper-rat P150; shRNA targeting sequence gatcgagagacagtcatca	Kononenko et al., 2017	N/A
pSuper-rat EB1/3; shRNAs targeting sequences tctgacaaagatagaacag / actatgatggaaaggattac	Kind gift from Dr. Anna Akhmanova; Komarova et al., 2005; Jaworski et al., 2009	N/A
pSuper-rat RTN1; shRNA targeting sequence gcagaggcctgtaaatata	This study	N/A
pSuper-rat RTN2; shRNA targeting sequence tagcacagaccaatcagaa	This study	N/A
pSuper-rat RTN3; shRNA targeting sequence ctgcaaatcgatgtattaa	This study	N/A
pSuper-rat RTN4; shRNA targeting sequence gtccagatttctctaatta	This study	N/A
pSuper-rat DP1; shRNA targeting sequence gacatataaagttccagaa	This study	N/A
pSuper-rat P180; shRNA targeting sequence tcagtgcaattgtctgtat	This study	N/A
pSuper-rat KTN1; shRNA targeting sequence ggaccttctcaagaggtta	This study	N/A
pSuper-rat CLIMP63; shRNA targeting sequence tcaaccgtattagtgaagttctaca	Targeting sequence from Cui-Wang et al., 2012	N/A
pSuper-mouse RTN4; shRNA targeting sequence gtccagagttctctaatta	This study	N/A
pSuper-mouse DP1; shRNA targeting sequence gagttcgtgcagcaattat	This study	N/A
Software and Algorithms		
ImageJ	NIH	https://imagej.nih.gov/ij/
ComDet	GitHub	https://github.com/ekatrukha/ComDet
GraphPad Prism	GraphPad Software INC	https://www.graphpad.com/scientific-software/

CONTACT FOR REAGENT AND RESOURCE SHARING

Further information and requests for resources and reagents should be directed to and will be fulfilled by the Lead Contact Casper Hoogenraad (c.hoogenraad@uu.nl).

EXPERIMENTAL MODEL AND SUBJECT DETAILS

Animals

All experiments were approved by the DEC Dutch Animal Experiments Committee (Dier Experimenten Commissie), performed in line with institutional guidelines of University Utrecht, and conducted in agreement with Dutch law (Wet op de Dierproeven, 1996) and European regulations (Directive 2010/63/EU). Female pregnant Wistar rats were obtained from Janvier, and embryos (both genders) at E18 stage of development were used for primary cultures of hippocampal and cortical neuron. Pregnant C57BL/6 mice were obtained from Janvier, and embryos (both genders) at E14.5 stage of development were used for ex-vivo electroporation and organotypic brain slice cultures.

Primary neuronal cultures and transfection

Primary hippocampal and cortical neurons cultures were prepared from embryonic day 18 rat brains. Cells were plated on coverslips coated with poly-L-lysine (37.5 μg/mL) and laminin (1.25 μg/mL) at a density of 100,000/well or 50,000/well (12-well plates). Neurons

were cultured in Neurobasal medium (NB) supplemented with 1% B27 (GIBCO), 0.5 mM glutamine (GIBCO), 15.6 μM glutamate (Sigma), and 1% penicillin/streptomycin (GIBCO) and maintained in an incubator under controlled temperature and CO2 conditions (37°C, 5% CO2). In most experiments, hippocampal neurons were transfected with different plasmid constructs using Lipofectamine 2000 (Invitrogen). Briefly, DNA (0.05-2 μg/well) was mixed with 1.2 μL of Lipofectamine 2000 in 200 μL Opti-MEM, incubated for 20 min at room temperature, and then added to the neurons in NB at 37°C in 5% CO2 for 1 h. Next, neurons were washed with NB and transferred to their original medium and maintained at 37°C in 5% CO2 until imaging of fixation. Alternatively, hippocampal (200,000 cells; 12 well plates) and cortical neurons (1,300,000 cells for Mass-Spectrometry experiments; 6-well plates) were nucleofected in suspension at DIV0 with different plasmid constructs using the Amaxa Rat Neuron Nucleofector kit (Lonza) according to the manufacturer's instructions.

Ex vivo electroporation and organotypic brain slice cultures

Embryonic mice brains were electroporated with 1.5μl DNA mixture containing a MARCKS-GFP vector plus shRNAs directed to RTN4 and DP1 or pSuper empty vector (control). DNA was dissolved in MQ with 0.05% FastGreen FCF Dye (Sigma). The mix was injected in the lateral ventricles of the embryonic brains using borosilicate glass micro-pipettes (World Precision Instruments) and a PLI-100A Picoliter Microinjector (Warner Instruments). Brain motor cortex were electroporated with platinum plated electrodes (Nepagene) using an ECM 830 Electro Square Porator (Harvard Apparatus) set to 3 unipolar pulses of 100ms at 30V with 100ms intervals. Embryonic heads were then isolated and collected in ice-cold cHBSS, embedded in 3% SeaPlaque GTG Agarose (Lonza) in cHBSS and sectioned coronally into 300 μm thick slices using a VT1000 S Vibratome (Leica). Slices were collected on poly-L-lysine and laminin-coated culture membrane inserts (Falcon), placed on top of slice culture medium (% v/v Basal Eagle Medium, 26% v/v cHBSS, 20mM D-glucose, 1mM L-glutamine, 0.1 mg/mL penicillin/streptomycin) and cultured 4 days prior to fixation.

Heterologous cell culture and transfection

African Green Monkey SV40-transformed kidney fibroblast (COS-7) cells from ATCC were cultured in DMEM/Ham's F10 (50%/50%) supplemented with 10% fetal calf serum and 1% penicillin/streptomycin at 37°C and 5% CO2. Cell lines were not authenticated by authors after purchase. The cell lines were routinely checked for mycoplasma contamination using LT07-518 Mycoalert assay (Lonza). Cells were plated in 18mm glass coverslips and transfected with Lipofectamine 2000 according to manufacturer's protocol.

METHOD DETAILS

DNA and shRNA Constructs

The following vectors were used: pEGFP(A206K)-N1 and pEGFP(A206K)-C1 (a gift from Dr. Jennifer Lippincott-Schwartz), pmCherry-N1 and mCherry-C1 (Clontech), pGW1-BFP (Kapitein et al., 2010), pSuper (Brummelkamp et al., 2002) and MARCKS-GFP (De Paola et al., 2003). GFP-KIF5A-Rigor was kindly provided by Dr. Juan Bonifacino (Farías et al., 2015), RTN4A-GFP was a gift from Dr. Gia Voeltz (Shibata et al., 2008; Addgene plasmid # 61807), GFP-ATL1 (Wang et al., 2016; Addgene # 86679) GFP-Sec61β (Addgene # 15108) and RFP-CLIMP63 were a gift from Dr. Tom Rapoport, GFP-P180 full length was a gift from Dr. Alice Ting (Hung et al., 2017; Addgene # 92150).

The following plasmids have been previously described: GFP-MACF43, named GFP-MT+TIP since it is used as a general marker to analyze the dynamics of microtubule growing plus-ends (Honnappa et al., 2009), RFP-TRIM46 (van Beuningen et al., 2015), GFP-CAMSAP2 (Yau et al., 2014), PA-GFP-α-Tubulin (Kuijpers et al., 2016), AnkG480-GFP (Fréal et al., 2016).

For the Strep/SBP heterodimerization system, Strep-KIFC1-HA and GFP- or mCh-SBP-RTN4A were generated. The region encoding amino acids 126-673 of KIFC1 was PCR amplified from KIFC1 cDNA (Clone I.M.A.G.E: 40117894) and the Streptavidin sequence was PCR amplified from mCh-KIF5A-MD-Strep (Farías et al., 2017). Both cDNAs were cloned into pmCherry-N1 between XhoI and SalI sites by GIBSON assembly. The mCherry sequence was removed and replaced by a 3x HA sequence, generated by oligos annealing and inserted between AgeI and BsrGI sites. A 3x(glycine-serine) linker was introduced between the Strep and KIFC1 sequences to allow freedom of movement between domains. The SBP sequence (DEKTTGWRGGHVVEGLAGELEQLRARLE HHPQGQREP), generated by oligo synthesis, was cloned into pEGFP(A206K)-C1 and pmCherry-N1 vectors, between XhoI and HindIII sites, to obtain the GFP-SBP and mCh-SBP plasmids. Then, RTN4A was PCR amplified from RTN4A-GFP (Shibata et al., 2008; Addgene plasmid # 61807) and cloned into GFP-SBP or mCh-SBP plasmids between SalI and BamH1 sites. A 3x(glycine-serine) linker was introduced between SBP and RTN4A sequences.

For the induced FRB/FKBP heterodimerization system, HA-BicD2-MD-FRB has been already described (Kapitein et al., 2010). To generate GFP-FKBP-RTN4 and mCh-FKBP-RTN4A, a 2x FKBP sequence was PCR amplified from PEX3-mRFP-FKBP (Kapitein et al., 2010) and RTN4A was PCR amplified from RTN4A-GFP (Shibata et al., 2008; Addgene plasmid # 61807). Both cDNAs were cloned into pEGFP(A206K)-C1 and pmCherry-C1 vectors, between XhoI and BamH1 sites by GIBSON assembly. A 3x(glycine-serine) linker was introduced between FKBP2x and RTN4A sequences.

Other plasmids obtained in this study includes: mCh-Sec61β, PCR amplified from GFP-Sec61β (Addgene # 15108) and cloned into pmCherry-SBP plasmid between SalI and BamH1 sites; GFP-KTN1, PCR amplified from Clone I.M.A.G.E: 40125683 and cloned into pEGFP(A206K)-C1 between XhoI and BamH1 sites; DP1-GFP, PCR amplified from Clone I.M.A.G.E: 6164621 and cloned into

pEGFP(A206K)-N1 between Sal1 and BamH1 sites; TRIM46 (from RFP-TRIM46; van Beuningen et al., 2015) was subcloned in pGW1-BFP.

All P180 deletion constructs were PCR amplified from P180 cDNA (Hung et al., 2017; Addgene #92150). P180Δcytosolic tail containing the luminal and transmembrane domain and the first 5 amino acids from the cytosolic tail followed by a 3x(glycine-serine) linker, were PCR amplified and cloned into pEGFP(A206K)-N1 vector between XhoI and BamH1 sites. The primers used to generate P180Δcytosolic tail plasmid are: 5′-agcgctaccggactcagatctcgagcaccatggatatttacgacactc-3′ and 5′-caccatggtggcgaccggtggatccg ggctaccgctgccgctacccatggagaaagtcgacac-3′. P180ΔCC containing all the luminal, transmembrane, and cytoplasmic domains (which lacks the coiled-coil region) followed by a 3x(glycine-serine) linker were PCR amplified and cloned into pEGFP(A206K)-N1 vector between XhoI and BamH1 sites. The primers used to generate the P180ΔCC plasmid are: 5′-agcgctaccggactcagatctcgagcaccatggatattt acgacactcaaac-3′ and 5′- caccatggtggcgaccggtggatccgggctaccgctgccgctaccagaagctgactctgtcttttac-3′. P180Δrepeats containing all the luminal, transmembrane, and cytosolic domain (lacking the decapeptide repeats region) were obtained by amplifying two PCR fragments, which were cloned into pEGFP(A206K)-N1 vector between XhoI and BamH1 sites by GIBSON assembly. One 3x(glycine-serine) linker was added between the two fragments and other between the coiled-coiled domain and GFP. The primers used to generate the P180Δrepeats domain are: 5′-agcgctaccggactcagatctcgagcaccatggatatttacgacactcaaaccttgg-3′ and 5′-ccgctgccgctaccagtgccagtggctggtgt-3′ for fragment 1, 5′-cactggcactggtagcggcagcggtagcgtccagggcagaaatacagatgtg-3′ and 5′ caccatggtggcgaccggtggatccgggctaccgctgccgctacccacgctggtgccctcctt-3′ for fragment 2.

The following rat-shRNAs were used in this study: KIF5A-shRNA (5′-gagacatcttcaaccacat-3′), KIF5B-shRNA (5′-tggagggtaaacttcatga-3′), KIF5C-shRNA (5′-tgagatctacttggacaaa-3′), KIF1A-shRNA (5′-cacgccgtcttcaacatca-3′), P150-shRNA (5′-gatcgagagacagtcatca-3′; Kononenko et al., 2017), EB1/EB3-shRNA (5′-tctgacaaagatagaacag-3′ and 5′-actatgatggaaaggattac-3′; Komarova et al., 2005; Jaworski et al., 2009), RTN1-shRNA (5′-gcagaggcctgtaaatata-3′), RTN2-shRNA (5′-tagcacagaccaatcagaa-3′), RTN3-shRNA (5′-ctgcaaatcgatgtattaa-3′), RTN4-shRNA (5′-gtccagatttctctaatta-3′), DP1-shRNA (5′-gacatataaagttccagaa-3′), P180-shRNA (5′-tcagtgcaattgtctgtat-3′), KTN1-shRNA (5′ ggaccttctcaagaggtta-3′) and CLIMP63-shRNA (5′-tcaaccgtattagtgaagttctaca-3′; Cui-Wang et al., 2012).

The following mouse-shRNAs were used in this study: RTN4-shRNA (5′-gtccagagttctctaatta-3′), and DP1-shRNA (5′-gagttcgtgc agcaattat-3′).

The shRNAs were developed using http://sirna.wi.mit.edu/. The oligonucleotides were annealed and inserted into pSuper vector.

Antibodies and reagents

The following antibodies were used in this study: rabbit anti-RTN4 (named Nogo; Novus, Cat# NB100-56681, RRID: AB_838641), mouse anti-RTN4 (named NogoA; R and D Systems, Cat# MAB3098, RRID:AB_10997139), mouse anti-KDEL (clone 10C3; Stressgen/Enzo, Cat# SPA-827, RRID: AB_10618036), mouse anti-Tau (clone PC1C6; Chemicon, Cat# MAB3420, RRID: AB_94855), chicken anti-MAP2 (Abcam, Cat# ab5392, RRID: AB_2138153), rabbit anti-TRIM46 (van Beuningen et al., 2015), mouse anti-AnkG (clone N106/36; UC Davis/NIH NeuroMab, Cat# 75-146, RRID: AB_10673030), mouse anti-Pan-Neurofascin external (clone A12/18; UC Davis/NIH NeuroMab, Cat# 75-172, RRID: AB_2282826), mouse anti-Sodium channel (Pan, clone K58/35; Sigma-Aldrich, Cat# S8809, RRID: AB_477552), rabbit anti βIV-Spectrin (Kind gif from Dr. Matthew Rasband), mouse anti-acetylated tubulin (Sigma-Aldrich, Cat# T7451, RRID: AB_609894), rabbit anti-detyrosinated tubulin (Millipore, Cat# AB3201, RRID: AB_177350), mouse anti-EB1 (clone 5/EB1; BD Transduction Laboratories, Cat# 610535, RRID: AB_397892), rabbit anti-CAMSAP2 (Proteintech, Cat# 17880-1-AP, RRID: AB_2068826), rabbit anti-GFP (Abcam, Cat# ab290, RRID: AB_303395), rabbit anti-GFP (MBL International, Cat#598S, RRID: AB_591816), mouse anti-GFP (3E6; Thermo Fisher Scientific, Cat# A-11120, RRID: AB_221568), mouse anti-mCh (Clontech Laboratories, Cat# 632543, RRID: AB_2307319), mouse anti-HA (Roche, Cat# 11666606001, RRID: AB_514506), donkey anti-mouse Alexa488 (Molecular Probes, Cat# A21202, RRID: AB_141607), donkey anti-mouse Alexa555 (Molecular Probes, Cat# A31570, RRID: AB_2536180), donkey anti-mouse Alexa647 (Molecular Probes, Cat#A31571, RRID: AB_162542), donkey anti-rabbit Alexa488 (Molecular Probes, Cat# A21206, RRID: AB_141708), donkey anti-rabbit Alexa555 (Molecular Probes, Cat# A31572, RRID: AB_162543), donkey anti-rabbit Alexa647 (Molecular Probes, Cat# A31573, RRID: AB_2536183), goat anti-chicken Alexa647 (Molecular Probes, Cat# A21449, RRID: AB_2535866), goat anti-mouse Alexa405 (Molecular Probes, Cat# A31553, RRID: AB_221604), goat anti-rabbit Alexa405 (Molecular Probes, Cat# A31556; RRID: AB_221605).

Other reagents used in this study were taxol (paclitaxel; Sigma-Aldrich, Cat# T7402), nocodazole (Sigma-Aldrich, Cat# 1404), rapalog (Takara, Cat# 635057), NeutrAvidin (Thermo Fisher Scientific, Cat#31000), Lipofectamine 2000 (Invitrogen, Cat#1639722), DiOC6(3) (3,3′-Dihexyloxacarbocyanine Iodide; Thermo-Fisher Scientific, Cat# D273), ER-Tracker Red (BODIPY TR Glibenclamide; Thermo-Fisher Scientific, Cat# E34250); Mix-n-Stain CF640R (Biotium, Cat# 92245), and FastGreen FCF Dye (Sigma, Cat# F7252).

Drug treatments

Nocodazole was used at 10 μM for 1h (Figure 3G) or 4h (Figures 3D, 3F, and 3H and Figure S4), taxol was used at 20nM for 4h (Figures 3D and 3I) or 16h (Figure 5H) or 72h for multiple axon formation experiments (Figures 5A and 7H). For induced FKBP/FRB heterodimerization assay, rapalog was used at 100 nM for 1h (Figures 4A and 4C–4J and Figures S5A–S5E). For the Strep-SBP heterodimerization system, NeutrAvidin (0.3 mg/mL) was added just after transfection to prevent Strep-SBP dissociation by the presence of biotin in the neuronal medium (Figures 4B and 4D and 5I). DMSO (0.001%) and ethanol (0.1%) were used as vehicle control treatments.

Mass spectrometry

Sample preparation

Untransfected, pSuper-transfected and shRNAs-transfected (RTNs; DP1) cortical neurons (DIV5) were washed 3 times with PBS and lysed with lysis buffer (8 M Urea, 50 mM triethylammonium bicarbonate, plus EDTA-free protease inhibitor Cocktail). 50ug of proteins from each condition were reduced (5 mM DTT, 55°C, 30 min), alkylated (10 mM Iodoacetamide, 30 min in the dark) and sequentially digested by LysC (Protein-enzyme ratio 1:50, 37°C, 4 h) and trypsin (Protein-enzyme ratio 1:50, 37°C, overnight). Resulting peptides were then desalted using C18 solid phase extraction cartridges (Waters) and subjected to stable isotope TMT-6plex labeling according to manufacturer's instruction (Thermo Scientific). For labeling the following scheme was used: untransfected = TMT-126; pSuper = TMT-127; shRNAs for RTNs = TMT-128; shRNA for DP1 = TMT-131. Differentially labeled peptides were mixed in a 1:1:1:1 ratio based on LC-MS/MS base peak intensity of the separate channels, dried in a vacuum concentrator and reconstituted in 10% formic acid for subsequent fractionation. Peptides were fractionated using offline high pH (basic) reversed-phase chromatography prior to MS analysis.

Data analysis

Samples collected after fractionation were analyzed on a Q-Exactive mass spectrometer (Thermo Fisher Scientific, Bremen, Germany) coupled online to an Agilent UPLC 1290 system (Agilent Technologies). Peptides were loaded onto a trap column (Reprosil C18, 3 μm, 2 cm × 100 μm; Dr. Maisch) with solvent A (0.1% formic acid) and separated on an analytical column (Poroshell 120 EC C18, Agilent Technologies, 50 μm x 50 cm, 2.7 μm) using a 120 min linear gradient from 7%–30% solvent B (0.1% formic acid in acetonitrile). For data analysis, raw files were processed using Proteome Discoverer 1.4 (version 1.4.1.14, Thermo Scientific, Bremen, Germany). Database search was performed using the Uniprot rat database and Mascot (version 2.5.1, Matrix Science, UK) as search engine. Carbamidomethylation of cysteines was set as a fixed modification. Oxidation of methionine and TMT-6plex of lysine residues and peptide N terminus, were set as variable modifications. Trypsin was set as cleavage specificity, allowing a maximum of 2 missed cleavages. Data filtering was performed using percolator, resulting in 1% false discovery rate (FDR). Additional filters were search engine rank 1 and mascot ion score > 20. Unique peptides or total peptides were used for quantification and the obtained ratios were normalized to the median. The mass spectrometry proteomics data have been deposited to the ProteomeXchange Consortium via the PRIDE partner repository with the dataset identifier PXD012264.

Immunofluorescence staining and imaging

Cells were fixed with 4% paraformaldehyde plus 4% sucrose in PBS for 20 min, permeabilized with 0.2% Triton X-100 for 15 min, blocked with 0.2% porcine gelatin for 30 min at 37°C, and stained with primary antibodies for 30 min at 37°C, followed by secondary antibodies for 30 min at 37°C. Cells were washed 3 times for 5 min in PBS after incubation with primary and secondary antibodies. For EB1 and CAMSAP2 staining, neurons were fixed with methanol (100%) containing 1mM EGTA for 10 min at −20°C followed by 4% paraformaldehyde plus 4% sucrose for 5 min. All fluorescence images were obtained using a confocal laser-scanning microscope (LSM700, Zeiss) equipped with a Plan-Apochromat 63x NA 1.40 oil DIC, EC Plan-Neofluar 40x NA1.30 Oil DIC and a Plan-Apochromat 20x NA 0.8 objectives. For fluorescence intensity comparison, settings were kept the same for all conditions. Organotypic culture of brain slices were fixed with 4% paraformaldehyde in PBS and then permeabilized and blocked in 10% normal goat serum/0.2% Triton X-100/PBS. Staining were performed by incubation with a rabbit anti-GFP antibody (MBL International) overnight at 4°C, followed by anti-rabbit conjugated with Alexa488 antibody plus DAPI overnight at 4°C. Slices were washed 4 times for 15 min in PBS after incubation with primary and secondary antibodies. Then, slices were mounted using Vectashield mounting medium (Vector Laboratories). Imaging of the whole neocortical region was performed in a LSM700 (Zeiss) confocal microscope equipped with a Plan-Apochromat 20x NA 0.8 objective with a 0.5x magnification. A total of 50-100 images (for each of the ~300 μm thick slices) were acquired, and maximum intensity projections were generated for analysis.

Live-cell imaging

All live-cell imaging experiments were performed in an inverted microscope Nikon Eclipse Ti-E (Nikon), equipped with a Plan Apo VC 100x NA 1.40 oil and a Plan Apo VC 60x NA 1.40 oil objective (Nikon), a Yokogawa CSU-X1-A1 spinning disk confocal unit (Roper Scientific), a Photometrics Evolve 512 EMCCD camera (Roper Scientific) and an incubation chamber (Tokai Hit) mounted on a motorized XYZ stage (Applied Scientific Instrumentation) which were all controlled using MetaMorph (Molecular Devices) software. Coverslips were mounted in metal rings and imaged using an incubation chamber that maintains temperature and CO2 optimal for the cells (37°C and 5% CO2). Imaging was performed in the original full conditioned medium from neurons in culture. For single-color videos, a laser channel used to visualize a specific fluorescently tagged protein was exposed for 100–200 ms. For dual-color videos, different laser channels used to visualize fluorescently tagged proteins were sequentially exposed for 100–200 ms. Total time and intervals of imaging acquisition for each experiment are indicated in each legend for Figure and/or legend for Movie. To identify the axon, neurons were stained live with a CF640R-conjugated antibody to the AIS protein neurofascin (Farías et al., 2015).

Fluorescence recovery after photobleaching and photo-activation

For GFP-Sec61β, RTN4A-GFP and ER-BODIPY red tracker photobleaching, the experiments were performed using the ILas2 system (Roper Scientific). Different regions of the neuron (indicated in each figure legend) were bleached with high laser power after 5 s

of recording, and fluorescence recovery was analyzed for a period of 5 min with imaging acquisition every 1 s. Photoactivation of PA-GFP-α-Tubulin was performed on the FRAP setup and achieved by scanning the desired region 3 times at 6%–10% laser power with a Vortran Stradus 405 nm (100 mW) laser. Photoactivation was performed ~1 min before imaging acquisition every 1 min for 1 or 4 h, as indicated in figure legends.

Streptavidin/SBP heterodimerization system assay

The forced coupling of cargoes to MT-driven motors has been described previously (Farías et al., 2015, 2017). Briefly, hippocampal neurons were transfected with HA-KIFC1-MD-Strep plus GFP-SBP-RTN4A at DIV6 and imaged at DIV7 (Figure 4B). Alternatively, hippocampal neurons were nucleofected in suspension at DIV0 and imaged at DIV2 (Figure 5I). Strep-SBP uncoupling was prevented by adding NeutrAvidin to the cell medium after 1h of transfection.

Drug-induced FKBP/FRB heterodimerization system assay

The inducible cargo trafficking assay was performed as describe previously (Kapitein et al., 2010). Briefly, hippocampal neurons were transfected with HA-BicD-MD-FRB plus GFP or mCh-tagged FKBP-RTN4A at DIV4-5 and imaged at DIV6-7. To induce specific binding of FRB and FKBP constructs, rapalog was added to a final concentration of 100nM for 1h. The heterodimerization system was co-transfected with GFP-Sec61β, GFP-ATL1 or GFP-DP1 plus fill (Figure 4C and Figure S5A-D), RFP-TRIM46 (Figure 4E), BFP-TRIM46 (Figure S6B-E) or BFP-TRIM46 plus AnkG480-GFP (Figure S6F), GFP-MT+TIP (Figure 4G), GFP-CAMSAP2 (Figure 4I), or PA-GFP-Tub (Figure 4J). For live cell imaging, neurons were incubated with rapalog and immediately recorded every 1-2min for 1h.

Labeling of ER membrane in fixed and live neurons

A stock solution of 0.5mg DiOC6(3) (3,3′-Dihexyloxacarbocyanine Iodide) in ethanol was prepared, aliquoted, and keep it at −20°C. Fixed neurons were immediately incubated for 10 s at room temperature with fresh dilution of 2.5 μg/mL DiOC6(3) (3,3′-Dihexyloxacarbocyanine Iodide) in PBS, and then cells were washed 4 times with PBS before imaging (Figures S2A, S2B, S4A, and S5A). A stock solution of 1mM ER-Tracker Red (BODIPY TR Glibenclamide) in DMSO was prepared, aliquoted, and keep it at −20°C. Live neurons were washed twice with HBSS/calcium/magnesium, immediately incubated with 1μM ER-Tracker Red in HBSS/calcium/magnesium for 30 min at 37°C, and then washed 3 times before imaging live in HBSS/calcium/magnesium medium (Figures S2C–S2E).

Image analysis and quantification

Data were collected and analyzed from 3-5 independent experiments. No specific strategy for randomization and/or stratification was employed. The studies were blind in data analysis.

Fluorescence line intensity plots

The distribution of different proteins was analyzed by using ImageJ. Plot profiles were generated from segmented lines traced along the transitional zone from the soma to the axon (Figures 2D, 3C, and 4C), or from proximal axon to medium-distal axon (Figures 3A, 3B, and 6E), or from initial to distal part of neurites of neurons at stage 2-3 (Figure 5E). A segmented line was also traced from the periphery to the perinuclear region of a COS7 cell to generate the plot profile shown in Figure 7B. Representative images and their corresponding plots are shown in each figure.

Polarity index

Several segmented lines were traced along three dendrites and one portion of the axon captured in each image. Mean intensities in these regions were calculated using ImageJ. The mean intensities from the three dendrites were averaged and used to calculate the polarity index (PI). The following formula was used $PI = (Id - Ia)/(Id + Ia)$:, where Id is the mean dendrite intensity and Ia is the mean axonal intensity. Non-polarized proteins present a PI = 0 (Id = Ia), whereas PI > 0 or PI < 0 indicates polarization toward dendrites or axons, respectively.

Kymograph analysis

Kymograph from live cell imaging were generated using ImageJ, as previously described (Farías et al., 2015). Briefly, segmented lines of several thickness and length were traced from the soma to the axon (Figures 2K and 4E), along dendrite (Figures 3G and 5H), along axon (Figures 3G, 3H, and 4J), or along neurite during axon formation and elongation (Figures 5F and 5G). Kymographs were generated from straightened lines by re-slicing stacks followed by z projection. All tracks were orientated so that anterograde movement occurred from left to right. Length of segmented line, as well as time of recording are shown in each kymograph.

Quantification of protein displacement

The shift in the distribution of RFP-TRIM46, GFP-CAMSAP2 and PA-GFP-Tub in neurons expressing the rapalog system imaged live for 1h, were analyzed by kymographs. Segmented lines were traced from the soma to the axon (Figure 4E), from the soma to the proximal segment of all neurites (Figure 4I), or within the proximal axon (Figure 4J) to measure the displacement per neuron and to calculate the mean shift between 0 min and 60 min of rapalog treatment. All of these proteins are remarkable stable in normal conditions, and their displacement is observed only in the presence of rapalog.

Quantitative FRAP analysis

The mean intensity of the bleached area was obtained and corrected with background values, as well as the bleaching that occurred during image acquisition. Data were normalized with control fluorescence averaged over 5 initial frames before bleaching and stated as 100% intensity. Average curves from several neurons were obtained and represented.

Quantitative PA-decay analysis

The mean intensity of the photoactivated area was obtained and corrected with background values. The mean intensity obtained from the first frame after photoactivation was stated as 1. Average curves from several neurons were obtained and represented.

Quantification of immunofluorescence intensity for endogenous proteins

All images were taken at the same settings for light and exposure with parameters adjusted so that the pixel intensities were below saturation. To determine intensities from endogenous staining of CAMSAP2 and acetylated tubulin in neurons or COS7 cells, a ROI was manually drawn around the neuronal soma for CAMSAP2 staining (Figure 4H), along the first 150 μm of axon (Figure 7F) or around individual COS7 cells (Figure 7C) for acetylated tubulin staining, and the mean intensity in the selected area was measured using ImageJ. Intensities were averaged over multiple cells and normalized to intensities in control cells.

Quantification of immunofluorescence intensity ratios in different regions of neurons

Several segmented lines were traced along three dendrites and one portion of the axon and a ROI was drawn around the soma for each image. Mean intensities in these regions were calculated using ImageJ. The sum of three regions (axon + dendrite + soma mean intensities) was expressed as value 1 (Figures 3E and S3A). For axon tip / soma intensity ratios, 4-8 ROIs were drawn around axonal tips and then averaged, and 1 ROI was drawn around the soma for each image. Value 1 correspond to average axon tip / soma intensity ratio in control condition (Figure S1A).

Quantification of EB-1 and MT+TIP -comets

ImageJ plugin ComDet (https://github.com/ekatrukha/ComDet) was used to quantify the number of EB1 or MT+TIP -comets in the soma of neurons (Figures 4F and 4G, respectively), or number of EB1 comets in individual COS7 cells (Figure 7D). Numbers were normalized to the corresponding area and averaged over multiple cells.

Quantification of ex-vivo neuronal migration

The degree of neuronal migration was quantified by measuring the positions of the cell bodies of GFP-positive neurons within the cortex, using the Analyze Particle plugin from ImageJ. The relative position of neurons in the regions of interest was recorded in terms of distance between the ventricle and the pial surface. The position information, including neurons across the entire Z series in the entire electroporated neocortial region together with the top (pial surface) and bottom (ventricle) boundaries, were imported to Excel. Based on the relative position of each neuron and the total numbers of neurons counted, the radial cell distribution along the radial axis was obtained by further data processing using an Excel macro and expressed as percentage of migration.

QUATIFICATION AND STATISTICAL ANALYSIS

All statistical details of experiments, including the definitions and exact values of n, and statistical tests performed, are shown in Figures and Figure Legends. n represent the number of analyzed cells from at least three independent experiments. Data processing and statistical analysis were done in Excel and GraphPad Prism (GraphPad Sofware). Significance was defined as: ns-not significant, $*p < 0.05$, $**p < 0.01$, and $***p < 0.001$. Statistical analysis includes: unpaired t test, pared t test, one-way ANOVA followed by a Dunnett's multiple comparison test, Kruskal–Wallis test followed by a Dunn's multiple comparison Test, and Wilcoxon signed-rank test. The assumption of normality was checked using D'Agostino-Pearson omnibus test.